Short title: Root hydraulic architecture and axial transport

Author for Contact: Christophe Maurel (christophe.maurel@cnrs.fr)

Phenotyping and modeling of root hydraulic architecture reveal critical determinants of axial water transport

Yann Boursiac[1†], Christophe Pradal[2,3,4†], Fabrice Bauget[1‡], Mikaël Lucas[1‡§], Stathis Delivorias[1], Christophe Godin[3¥], Christophe Maurel[1*]

[1]Institute for Plant Sciences of Montpellier (IPSiM), Univ Montpellier, CNRS, INRAE, Institut Agro, Montpellier, France.

[2]CIRAD, UMR AGAP Institut, Montpellier, France.

[3]Inria Project-team Virtual Plants, UMR AGAP, Univ Montpellier, INRIA, CIRAD, INRAE, Montpellier, France.

[4]Inria & LIRMM, Univ Montpellier, CNRS, Montpellier, France

[†]These authors contributed equally to the work

[‡] These authors contributed equally to the work

Present addresses : [§]UMR DIADE, Univ Montpellier, IRD, Montpellier, France ; [¥]Laboratoire Reproduction et Développement des Plantes, Univ Lyon, ENS de Lyon, UCB Lyon 1, CNRS, INRAE, Inria, Lyon, France.

The author responsible for distribution of materials integral to the findings presented in this article in accordance with the policy described in the Instructions for Authors (https://academic.oup.com/plphys/pages/General-Instructions) is Christophe Maurel.

One-sentence summary: A model-assisted experimental dissection of architecture and water transport properties of Arabidopsis root systems reveals limiting roles of xylem transport.

Author contributions: Y.B. contributed to model coding, developed the cut-and-flow and root intercept approaches, and contributed to phenotyping characterizations; C. P. supervised the coding of the HydroRoot model and contributed to data analyses; F.B. finalized model coding, performed sensitivity analyses and contributed to cut-and-flow analyses; M.L. developed the first HydroRoot model version and performed root anatomy analyses ; S.D. performed the analysis of root intercept numbers; C.M. and C.G. designed the study which was regularly discussed with Y.B. and C.P.; C.M. wrote the article with contributions of all the authors.

Abstract

Water uptake by roots is a key adaptation of plants to aerial life. Water uptake depends on root system architecture (RSA) and tissue hydraulic properties that, together, shape the root hydraulic architecture. This work investigates how the interplay between conductivities along radial (e.g. aquaporins) and axial (e.g. xylem vessels) pathways determines the water transport properties of highly branched RSAs as found in adult Arabidopsis (*Arabidopsis thaliana*) plants. A hydraulic model named HydroRoot was developed, based on multi-scale tree graph representations of RSAs. Root water flow was measured by the pressure chamber technique after successive cuts of a same root system from the tip towards the base. HydroRoot model inversion in corresponding RSAs allowed us to concomitantly determine radial and axial conductivities, providing evidence that the latter is often overestimated by classical evaluation based on the Hagen-Poiseuille law. Organizing principles of Arabidopsis primary and lateral root growth and branching were determined and used to apply the HydroRoot model to an extended set of simulated RSAs. Sensitivity analyses revealed that water transport can be co-limited by radial and axial conductances throughout the whole RSA. The number of roots that can be sectioned (intercepted) at a given distance from the base was defined as an accessible and informative indicator of RSA. The overall set of experimental and theoretical procedures was applied to plants mutated in *ESKIMO1* and previously shown to have xylem collapse. This approach will be instrumental to dissect the root water transport phenotype of plants with intricate alterations in root growth or transport functions.

Introduction

Water uptake by roots represents a key adaptation of plants to aerial life. Taking place at the plant soil interface, this process is highly dependent on the root system architecture (RSA). Most root systems are highly complex, branched structures with, for instance, thousands of ramifications and a cumulated length of several hundreds of meters for a single maize (*Zea mays*) plant. These systems are also highly dynamic. In particular, water availability interferes with the orientation and rate of primary root growth and the frequency and symmetry of root branching thereby promoting water resource foraging (Klein et al., 2020; Maurel and Nacry, 2020). The ability of root systems to reach deep soil layers at reduced cost was proposed to be a key trait for acclimation to water deprived environments (Lynch, 2013). Yet, a comprehensive view of how elementary water transport processes occur in root tissues and integrate within the RSA, thereby shaping the root hydraulic architecture, is needed to fully comprehend the water uptake capacity of plants.

Water uptake and its subsequent transport within the plant are determined by the gradient of water potentials throughout the soil-plant-atmosphere-continuum (Draye et al., 2010; Steudle, 2001). Following radial transport across peripheral cell layers (epidermis, cortex, endodermis), soil water reaches the stele and xylem vessels where it is transported axially to the plant aerial parts. These radial and axial processes, that are often presented sequentially, actually operate simultaneously and throughout the whole RSA. In most physiological studies of root water transport, axial conductance was inferred from xylem vessel size using the Hagen-Poiseuille law (Klein et al., 2020; Lefebvre et al., 2011; Steudle and Peterson, 1998). Because it is the site for formation of xylem vessels, the root tip was identified as the main resistive place for axial water transport whereas axial limitation was supposedly negligible in older root segments due to the presence of large metaxylem vessels (Steudle and Peterson, 1998). In contrast, radial transport which is often represented as a combination of cell-to-cell and cell wall (apoplastic) paths running in parallel, was proposed to explain fundamental hydraulic properties of the whole root (Barrowclough et al., 2000; Knipfer and Fricke, 2011; Steudle and Peterson, 1998).

Several types of numerical hydraulic models have been developed to address the complexity of root water uptake, and radial transport in particular. Whereas early models integrated concentric hydraulic resistances within a root radial section (Bramley et al., 2009; Jones et al., 1988; Steudle and Jeschke, 1983), modelling was recently applied to a more precise, cell-based view of the root radial anatomy (Couvreur et al., 2018; Heymans et al., 2021). Biophysical models have also addressed water transport at whole root level. With respect to models that describe the functioning of root segments (Frensch and Steudle, 1989; Zarebanadkouki et al., 2014; Zwieniecki et al., 2003) or use a simplified representation of root system hydraulics (Knipfer and Fricke, 2011), Doussan and colleagues integrated an explicit description of RSA with hydraulics. To be linked to soil water transfer, hydraulic

87 functioning of the root had, however, to be reduced to simplified radial and axial processes (Doussan
88 et al., 1998a; Doussan et al., 1998b). Since then, there have been several attempts to refine the
89 hydraulic functioning of elementary root segments at the whole root level (Bouda et al., 2018; Draye
90 et al., 2010; Foster and Miklavcic, 2016; Javaux et al., 2013; Zwieniecki et al., 2003). More recently,
91 Meunier and colleagues (Meunier et al., 2017b; Meunier et al., 2017c) developed a hybrid analytical-
92 numerical model of root water uptake with increased computational efficiency.

93 Despite these efforts, the respective limitations of axial and radial conductances and their
94 precise contribution to whole root hydraulics remain key and as yet unresolved issues. Based on a
95 porous pipe representation of unitary roots, (Zwieniecki et al., 2003) showed that axial hydraulic
96 limitation can lead to saturation of root conductance meaning that long roots do not provide any
97 additional advantage in terms of overall flux intensity (Meunier et al., 2017a; Meunier et al., 2018;
98 Zwieniecki et al., 2003). This view was recently extended to entire root networks which, however,
99 remained theoretical in nature (Bouda et al., 2018). While these modeling approaches point to key
100 hydraulic properties of root systems, most of them were assessed with scarce or heterogeneous
101 experimental data.

102 With respect to native, soil-imbedded root systems, roots excised from hydroponically grown
103 plants are more easily amenable to accurate hydraulic measurements. In Arabidopsis (*Arabidopsis*
104 *thaliana*) in particular, the pressure chamber technique has proved efficient for addressing
105 fundamental root hydraulics properties in various genotypes or environmental conditions (Di Pietro
106 et al., 2013; Postaire et al., 2010; Sutka et al., 2011). More specifically, this technique provides access
107 to the whole root system hydraulic conductivity (Lp_r) and allows to take into account the contribution
108 of fragile lateral roots.

109 Here, we used pressure chamber measurements coupled with a modelling approach to
110 investigate how the interplay between radial and axial conductivities determines the water transport
111 properties of complex and realistic RSAs. By combining experimental and computational modelling
112 procedures, this work shows how radial and axial conductivities can be concomitantly determined
113 and reveals contexts in which axial conductance can be limiting. The overall approach can also help
114 dissect the root water transport phenotype of plants with complex alterations in root growth or
115 transport functions.

116 Results

117 Mapping hydraulic properties on realistic models of RSAs

118 We first explored a set of 10 three-week-old, hydroponically grown Col-0 plants for which root water
119 transport capacity was measured by the pressure chamber technique and RSA was captured by
120 image analysis (Figure 1A). The root systems of these plants exhibit a substantial complexity with

total length up to 2.1 m, and up to 354 root extremities corresponding to a primary root carrying two orders of lateral roots (Table 1). We described quantitatively the individual RSAs by constructing dynamical multi-scale tree graphs (MTG) (Godin and Caraglio, 1998). The graph nodes represented plant segments of 100 µm (equivalent to the range of a cell length) and contained information on the position of the different branching points (Danjon and Reubens, 2008; Godin et al., 1999; Lobet et al., 2015) (Figure 1B). Microscopic observations indicated that diameters of the primary and lateral roots were fairly homogeneous within each branching order but were reduced by 30-40% between successive orders, varying from 188 ± 22 µm (± SD; n=64) in the primary root to as low as 69 µm in second order lateral roots. Thus, external root surfaces were calculated in the MTGs, assuming that root diameter was constant for a given root order, with a 30% decrease between successive root orders.

Based on these detailed RSA representations, we developed a hydraulic model to simulate water fluxes in the corresponding segment network. In this model, called HydroRoot (https://github.com/openalea/hydroroot), each elementary root segment is associated with a derivative microcircuit containing both radial (*k*) and axial (*K*) hydraulic conductances. While the former (*k*) accounts for all pathways mediating radial water flow, the latter (*K*) represents the conductances of the segment xylem vessels (Figure 1C). Accordingly, each elementary root segment is connected with the root bathing solution, and with basal and apical neighboring segments (Figure 1C). Overall, an individual root is represented as a series of elementary units while root branching is considered as a derivation in the global circuit (Figure 1D). Moreover, root tips are considered as terminal segments, with an elementary radial flow that feeds into the axial flow of the neighboring segment. In addition, endogenous osmotic driving forces were not taken into account since spontaneous exudation was close to 0 in our conditions (Boursiac et al., 2005). Thus, the boundary variables of the hydraulic model are either imposed experimentally [homogeneous water potential (hydrostatic pressure) in the bathing solution; root base at equilibrium with atmospheric pressure] or are measured [outgoing water flow: $J_v(P)$]. Based on these principles, HydroRoot can be run through a two-pass algorithm throughout the RSA, as previously described on aerial branching structures (Prusinkiewicz et al. 2007): equivalent conductances of the different branches are first computed in a backward pass (from root tips to base), followed by a forward pass (from root base to tips) computing the water potentials at each point of the root system. Due to the lack of capacitive components, water fluxes entering each elementary unit through radial or axial transport are equilibrated by the out-going axial flux toward the root base. The set of model parameters is recapitulated in Supplemental Table 1.

154 **Parameterization of axial conductance (*K*) for deduction of root radial conductivity (*k*)**

155 To parameterize axial conductances, xylem vessel number and size were sampled along the axis of
156 primary, first and second order lateral roots of five independently grown Col-0 plants. Supplemental
157 Figure 1A shows typical xylem differentiation patterns from root tip to base. Xylem conductance was
158 computed according to Hagen-Poiseuille law applied to the general case of elliptic conduits and
159 implemented according to vessel number and size in each elementary unit, thereby providing a
160 conductance profile along the root axis (Supplemental Figure 1B). Because it is linked to the 4th
161 power of vessel radius, *K* shows a dramatic increase (> 600 fold) from root tip to base. We found no
162 clear distinction between *K* profiles, in terms of shape and magnitude, among different root orders
163 and plants. Thus, a unique *K* profile derived from experimental data by locally weighted scatterplot
164 smoothing (lowess) was applied along all root axes (Supplemental Figure 1B).

165 The direct determination of *k* is, at present, experimentally not achievable in species with
166 highly branched and tiny roots such as Arabidopsis, as it would require to measure radial flows in
167 root segments between consecutive branching points (~2mm in the present case) (Meunier et al.,
168 2018). We therefore estimated radial conductance values by inverse modeling, using the RSA and
169 outgoing water flow [J_v(P)] data determined in the 10 plants described above. Considering that *k* is
170 constant from the root base to tips, its value was determined in individual plants, as presented in
171 Table 1, and ranged from 3.4 to 22.1 10^{-8} $m.s^{-1}.MPa^{-1}$, with an average of 10.4 ± 2.0 10^{-8} $m.s^{-1}.MPa^{-1}$ (±
172 SE).

173 **Concomitant determination of axial and radial conductances by model inversion**

174 Although based on well-established physical principles, the calculation of *K* presented above
175 overlooks the finite length of xylem vessels and neglects possible hydraulic limitations occurring
176 during water passage between adjacent vessels or at root branching sites (Shane et al., 2000).
177 Previous authors have also found discrepancies between calculated and measured axial conductance
178 (Bouda et al., 2018; Frensch and Steudle, 1989; Tixier et al., 2013). Here, we refined our approach to
179 simultaneously determine axial and radial conductances by model inversion in individual and real
180 RSAs. For this, we characterized root systems that were sequentially sectioned at a given distance
181 from their bases. The overall procedure is illustrated in Supplemental Figure 2A. Figure 2A and B
182 illustrates a series of pressure chamber measurements obtained after successive cuts of a same root
183 system from the tip towards the base. The successive cuts create direct hydraulic connections
184 between the cell bath and xylem lumen, and thereby J_v(P) increases although overall root surface
185 area progressively decreases (Supplemental Figure 2C, Figure 2A and B). For reference, control intact
186 roots systems that underwent the same successive pressurization cycles showed a constant J_v(P)
187 (Supplemental Figure 2B). Unlike previous analyses performed on elementary root segments

188 (Frensch and Steudle, 1989; Meunier et al., 2018), the present experimental procedure results in a
189 complex mix of sections of various root orders, made at the same distance from the root base, but at
190 varying distances from their respective tip (Supplemental Figure 2). Thus, we used a parameter
191 adjustment procedure on HydroRoot running with digitized architectures, either intact or with the
192 indicated sections, to infer *k* (set constant over the overall RSA) and *K* (as a piecewise linear function
193 of the distance to tip, see Materials and Methods). The robustness of the multi-parameter
194 adjustment procedure for *K,* almost independent of the first guess parameter values, is displayed in
195 Supplemental Figure 3. When applied to 10 individual RSAs, this so-called cut-and-flow approach
196 confirmed the variability in *K* profile previously observed between plants (Figure 2C). Most
197 importantly, it pointed to adjusted *K* values that were markedly lower than those calculated using
198 Hagen-Poiseuille law, by a factor of 4-6. In relation to these new *K* estimates, *k* values inferred from
199 the cut-and-flow approach were higher (mean value ± SE: 32.8 ± 6.5 10^{-8} $m.s^{-1}.MPa^{-1}$) than when
200 using the first inversion method described above (Figure 2D).

201 Since a constant radial conductivity (*k*) represents a strong assumption of our model, we also
202 investigated roots in which *k* was set constant in root tips but, due to suberization, dropped to a 3-
203 times lower plateau value in the differentiated zone (Doussan et al., 1998b; Heymans et al., 2021;
204 Ranathunge and Schreiber, 2011). Using such *k* profile and cut-and-flow data from the same 10
205 plants as above, we obtained a slightly but non-significantly reduced average plateau value of *k*
206 (Supplemental Figure 4A). Moreover, this non-uniform *k* profile did not significantly modify the
207 variation of *K* along the root axis (Supplemental Figure 4B). We interpret this to mean that the
208 increase in J_v(P) observed upon successive cuts of the RSA, and opening of vessels, is much more
209 powerful to capture spatial variations of axial conductance (*K*) than *k*.

210 **A general model of Arabidopsis RSA**

211 In order to explore the combined impacts of *k*, *K* and RSA on root water transport, we went on to
212 apply the HydroRoot model to an extended, yet realistic, set of simulated RSAs. Our first step was
213 therefore to develop a general model of Arabidopsis RSA.

214 To do this, we first explored the organizing principles of Col-0 RSA by observing primary and
215 first and second order lateral roots in a set of 13 individual plants. When looking at the distribution of
216 root branching, we observed that this process was always initiated between 8 and 40mm from the
217 root tip, and then developed at a relatively stable rate, which was similar between the primary root
218 and the lateral roots (Figure 3A). Thus, the cumulated number of lateral roots that have emerged at a
219 given distance of any root tip can be described by a linear relationship defined by a nude tip length
220 and a slope determined by the average internode length.

221 Next, we investigated the length of lateral roots with respect to their position along the
222 parental axis. The scattered data indicated a progressive but stochastic growth of laterals on the
223 bearing axis (Figure 3B). Yet, first order lateral roots showed a more pronounced growth than second
224 order lateral roots at a same distance of their respective parental root tip. We therefore established
225 distinct length laws for the two orders of lateral roots.

226 These observations allowed us to deduce the parameters of a root model that can be used to
227 generate RSAs. Using realistic ranges of nude tip length (between 5 and 35mm) and average
228 internode length (1-2.75mm), we modeled the stochastic process of lateral root branching by a first-
229 order Markov chain on growing root axes (Lucas et al., 2008). In addition, the length of simulated
230 lateral roots was determined by fitting lateral root length along parental root axes (Figure 3B). Root
231 diameters were set for each root order as indicated above. Setting the primary root length between
232 4 and 20 cm, we generated 9520 RSAs that spanned the whole range of input parameters. Figure 3C
233 illustrates the diversity of RSAs that can be generated using this pipeline.

234 **Capturing features of RSAs using patterns of intercepted roots**

235 In line with the cut-and-flow approach, we noted that phenotyping real RSAs by counting the number
236 of roots that can be sectioned (intercepted) at six distances from their base (*e.g.* 80, 60, 45, 30, 20,
237 10 mm) was at least five times as fast as a full RSA reconstruction. The latter needs determining the
238 nude tip length, position and length of all lateral roots. By comparison, the number of intercepted
239 roots at a few given distances from the base seems to be a more accessible yet informative indicator
240 of RSA. Figure 4A illustrates intercept number curves derived from discrete cuts in real RSAs or from
241 digitized Col-0 RSAs. These curves are overlapping with analogous intercept number curves, but
242 derived from simulated RSAs.

243 Analysis of the full data set showed that cumulated intercepts were significantly correlated
244 to architectural parameters of the root, such as the total root length (Supplemental Figure 5A).
245 Another feature of these curves is that they cumulate intercept distributions of first and second
246 order lateral roots thereby capturing a key aspect of root branching (Figure 4B).

247 Finally, we wondered about the capacity of a determined intercept number profile to
248 distinguish between markedly different RSAs. Supplemental Figure 5B shows a set of simulated RSAs
249 that share intercept number profiles similar to those of reference real RSAs. The simulated RSAs
250 were indeed very close, although with some variation, in their total root length (Figure 4C). The
251 overall data establish that intercept number profiles allow to capture some fundamental features of
252 RSAs.

253 **Sensitivity analysis of root water transport to architecture and hydraulic parameters**

254 Next, we applied the HydroRoot model to calculate the sap flow at a driving pressure of 0.3MPa
255 [J_v(0.3MPa)] in our collection of simulated RSAs using three distinct, yet realistic hydraulic
256 configurations. For this, we selected three contrasting but uniform *k* values, all derived from cut-and-
257 flow experiments, and applied a varying multiplying factor (*ax*) to the median axial conductivity (*K*)
258 profile determined in the same approach (see Figure 2C). Thus, in addition to an intermediate
259 hydraulic configuration (mean *k* value: 32.8 10^{-8} m.s^{-1}.MPa^{-1}; *ax*=1), we defined a low hydraulic
260 (minimal *k* : 9.9 10^{-8} m.s^{-1}.MPa^{-1}; *ax*=0.5) and a high hydraulic (maximal *k* : 71.4 10^{-8} m.s^{-1}.MPa^{-1}; *ax*=2)
261 setting. The three sets of simulations derived from these settings show a large range of J_v(0.3MPa)
262 values for RSAs of varying size (surface) and encompass the 20 experimentally determined J_v(0.3MPa)
263 values (Figure 5A).

264 The whole set of simulated RSA was used to explore the overall sensitivity of root water flow
265 to elementary input architectural parameters. A dependency of J_v(0.3MPa) on primary root length
266 (Figure 5B) and average internode length (Figure 5C) can be observed whereas nude tip length
267 (Figure 5D) had no impact on simulated flow. In the latter case, this means that the presence or
268 absence of relatively short lateral roots close to the tip has a negligible impact on J_v(0.3MPa). Finally,
269 when the intermediate hydraulic setting was used, the variation range of all input architectural
270 parameters was responsible for a variation of J_v(0.3MPa) by about one order of magnitude.

271 J_v(0.3MPa) was also dependent on variations in hydraulic parameters (Figure 6). Using the set
272 of 9520 simulated RSAs described above, we observed a positive and slightly saturating relationship
273 between J_v(0.3MPa) and *k* (Figure 6A and 6B; Supplemental Figure 6A). A similar behavior was
274 observed when varying *ax* values were applied to the whole axial conductivity (*K*) profile (Figure 6A
275 and 6C; Supplemental Figure 6B). These behaviors were not independent since sensitivity of
276 J_v(0.3MPa) to *k* or *ax* was higher and the saturation plateau was more pronounced when reference
277 *ax* or *k* parameters were set to lower values (Figure 6A; Supplemental Figure 6). Thus, J_v(P) seems to
278 be co-limited by the radial and axial conductivity in a large range of values.

279 The strong dependence of *K* on vessel diameter, as indicated by Hagen-Poiseuille law, is
280 usually interpreted to mean that the small vessels present at root tips are by far the most limiting
281 (Steudle and Peterson, 1998). To examine this point in detail, we inspected the spatial variation of
282 sap flow when a constant reducing factor (*ax* < 1) was applied throughout the *K* profile.
283 Supplemental Figure 7 illustrates this approach on a representative RSA. Figure 6D summarizes the
284 results, showing the relative variation of primary root axial flow at the indicated distance from root
285 tip, under varying *ax* values. Although flow sensitivity was the highest close to root tip, we observed,
286 for moderate axial limitations (0.5<*ax*<1), a pronounced and somewhat comparable impact of *ax*
287 variation on axial flow all along the root. Thus, limitation of axial conductivity appears to be

288 distributed over the whole primary root length. Since converging flows in a highly branched
289 architecture may create marked hydraulic constraints in basal root sections, we also considered the
290 simpler case of a cylindrical root harboring the same *K* profile as above (dashed lines, Figure 6D).
291 Although axial flow was less sensitive to axial limitation (*ax* < 1) than in highly branched roots, a flow
292 limitation along the whole root axis was also observed. These results emphasize the functional
293 relevance of profiles with increasing *K* along the whole root axis, as determined by the cut-and-flow
294 approach (Figure 2C).

295 We then investigated possible interactions between hydraulic and architectural parameters
296 in determining root water transport capacity (Supplemental Figure 8). For comparison of different
297 hydraulic settings, corresponding J_v(0.3MPa) flow values were centered using a normalizing factor. In
298 such analyses, the relative response of J_v(0.3MPa) to architectural input parameters was very similar
299 between high (k=71.4 10^{-8} m.s^{-1}.MPa^{-1}; *ax*=5) and low (k=9.9 10^{-8} m.s^{-1}.MPa^{-1}; *ax*=0.01) hydraulic
300 settings (Supplemental Figure 8).

301 Finally, we investigated the preferential sites of water uptake predicted in a whole root
302 placed in a pressure chamber. Figure 6E represents a heatmap of simulated radial inflow (j_i, Figure
303 1C) throughout a typical RSA. Under intermediate hydraulic conditions (k = 32.8 10^{-8} m.s^{-1}.MPa^{-1};
304 *ax*=1), the highest radial flow is observed at the vicinity of the root base, in the primary root as well
305 as the first order lateral roots (Figure 6 E, middle). A similar pattern is observed after increasing two-
306 fold the axial conductance (*ax* = 2; Figure 6E, right). In contrast, water uptake by first order lateral
307 roots and downstream roots was strongly reduced under lower axial conductance (*ax* = 0.125; Figure
308 6E, left). When a non-uniform *k* profile was used (*k* was the highest in root tips and dropped 3 times
309 to a lower plateau value in the differentiated zone; see above), radial inflow was enhanced in root
310 tips but the remaining spatial pattern was comparable to that with uniform *k* (Supplemental Figure
311 4C). Overall, these analyses illustrate how the axial conductance can influence the whole root
312 hydraulic architecture, and determines the relative contribution of the root basal and distal parts to
313 whole root water uptake.

314 **Dissecting the root hydraulic architecture of *esk1* mutants**

315 ESKIMO1 (ESK1) is a xylan-specific O-acetyltransferase (Yuan et al., 2013) which interferes with
316 cellulose fibril organization and deposition of plant secondary cell walls. As a consequence, *esk1*
317 mutants exhibit an irregular xylem (*irx*) syndrome (Lefebvre et al., 2011). Here, we decided to re-
318 examine the hydraulic defects observed in these mutants (Lefebvre et al., 2011) with a
319 comprehensive analysis of their root hydraulic architecture, based on the numerical approach
320 developed above. Morphological inspection of real plants of two allelic mutants of *ESK1* (*esk1-1*,
321 *esk1-5*) showed root growth alterations. While primary root growth was not different between

genotypes, the intercept number profiles based on digitized RSAs of 7 *esk1-1* plants and 7 *esk1-5* plants highlighted, with respect to Col-0, a clear reduction in root density in the 25-75mm range from the base (Figure 7A and 7B). This is attributable to a reduction in length of first order laterals which translates into a deficit in second order laterals. Lefebvre et al. (2011) hypothesized from discrete anatomical cuts of the root that axial conductance might be reduced in *esk1*. We then used cut-and-flow experiments assisted by the HydroRoot model developed above to further characterize the hydraulic properties of *esk1* roots. The analyses indicated that the median *K* of *esk1-1* and *esk1-5* was markedly reduced compared to Col-0 by factors from 1.6 up to 19.1 along the primary root axis (Figure 7C). The cut-and-flow approach also allowed us to estimate *k*, which, by comparison to Col-0, appeared to be reduced by 55 % to 33 % in *esk1-1* and *esk1-5*, respectively (Figure 7D) and by 40 % (P= 0.11; Student's *t* test) in cumulated data from *esk1-1* and *esk1-5*. Thus, in complement of an earlier report (Lefebvre et al., 2011), our results suggest that the loss of *ESK1* function impacts not only xylem conductance, but also other determinants of root water transport capacity. More generally, this study shows how our model assisted phenotyping allows to dissect the Arabidopsis root hydraulic architecture into three major components (RSA, radial and axial conductivities), and analyze their interplay in various genotypes.

Discussion

Investigating Arabidopsis root hydraulic architecture

Over the last two decades, the Arabidopsis root has emerged as a model of choice to address molecular and physiological aspects of aquaporin regulation (Boursiac et al., 2008; Lee et al., 2012), and more recently, to dissect plant tissue hydraulics by means of quantitative genetics (Shahzad et al., 2016; Tang et al., 2018). Although produced in adult plants, the data were interpreted using a simplified representation of the root as a single, continuous barrier between two homogeneous compartments, e.g. the soil solution and the xylem sap (Javot et al., 2003). Thus, the complexity and organizing principles of RSA in these plants, and its impact on the root uptake capacity have not yet been addressed. By comparison, more elaborate root hydraulic models exist in other plant species such as maize and lupine (*Lupinus albus*) (Meunier et al., 2018; Zarebanadkouki et al., 2016), which are indeed more amenable than Arabidopsis to root water transport assays and anatomical dissection. With respect to these high-yielding crops, the wild species Arabidopsis exhibits moderate growth but comparable transpiration rates (Hosy et al., 2003; Macho-Rivero et al., 2017; Yang et al., 2012). Thus, it has been unclear whether its system of thin, highly branched roots is also hydraulically optimized for high water flows.

Here, we have investigated the organizing principles of Arabidopsis root hydraulic architecture, using interplay between experimental and computational modelling approaches. To ensure a maximal physiological meaning, experimental measurements and numerical simulations were performed at a water potential gradient (*i.e.* 0.3 MPa) consistent with water flows driven by transpiration under standard growth conditions. In addition, starting from a fine characterization of wild-type (Col-0) plants, our study was extended to possibly encompass a large panel of accessions and genotypes.

Our major concern was to understand the relative impact of elementary axial and radial hydraulic parameters on sap flow. Whereas confrontation of theoretical and experimental data through model sensitivity analysis remains the most common approach, there is a restricted number of studies whereby hydraulic parameters were deduced from inverse modelling and integration of architectural components (Doussan et al., 2006; Doussan et al., 1998b; Meunier et al., 2018; Pascut et al., 2021; Zarebanadkouki et al., 2016). While these earlier studies relied on functional analyses of individual axial roots of maize, lupine or Arabidopsis, we describe here a procedure based on cut-and-flow measurements for simultaneous determination of axial and radial conductance in highly branched root systems.

370 **Assessing radial conductance**

371 A direct experimental dissection of radial conductance components is, at present, not achievable. It
372 would require an exact knowledge of the water potential across the root section, and the
373 experimental determination of elementary hydraulic conductivities corresponding to different
374 transport pathways. Even though cell membrane permeability can be measured using cell pressure
375 probe or protoplast swelling assays (Hüsken et al., 1978; Ramahaleo et al., 1999), all cell types are
376 not amenable to these experimentations. Furthermore, the permeability of other components of
377 radial water transport, such as the apoplast, has not been clearly determined yet (Buttersack and
378 Basler, 1991). The present HydroRoot model proposes to synthetize the overall radial pathway
379 through a single radial conductance (*k*) value. Here, we used an inverse modeling scheme similar to
380 those developed in Arabidopsis and maize (Couvreur et al., 2018; Pascut et al., 2021) to determine *k*
381 from RSA, J_v(P) and *K*. In a simplified representation of Arabidopsis root anatomy, the outer tissues
382 can be reduced to 3 concentric cylinders (cell layers) corresponding to the epidermis, cortex and
383 endodermis, with 6 cellular membranes in series. Cell pressure probe measurements in Col-0 cortical
384 cells have given a cell membrane hydraulic conductivity of 1-4 10^{-6} $m.s^{-1}.MPa^{-1}$ (Boursiac et al., 2008;
385 Sutka et al., 2011). We note that the order of magnitude of *k* determined in this work by inverse
386 modelling (3 10^{-7} $m.s^{-1}.MPa^{-1}$) fits with 1/6th of this range, in agreement with the idea that radial
387 water transport in the Arabidopsis root is predominantly mediated through cell membranes
388 (aquaporins)(Tournaire-Roux et al., 2003).

389 Another line of simplification of HydroRoot is that, in most of our simulations, *k* was set
390 constant from the root tip to base. Besides its simplicity, this hypothesis is supported by several
391 studies, including a hydraulic dissection of developing maize roots through segment analysis (Frensch
392 et al., 1996) and a hydraulic model inversion approach (Meunier et al., 2018) in young lateral and
393 seminal roots of maize and lateral roots of lupine. Yet, plant roots show a progressive development
394 of endodermal and peridermal barriers (Calvo-Polanco et al., 2021; Campilho et al., 2020; Doblas et
395 al., 2017; Ranathunge and Schreiber, 2011) and longitudinal variations in aquaporin gene expression
396 (Gambetta et al., 2013). Measurements of water uptake profiles in lupine or maize roots have also
397 suggested a steady decrease of *k* over root length (Doussan et al., 1998b; Zarebanadkouki et al.,
398 2016). Here, we investigated a two-step radial conductivity profile with a constant value of 3 *k* from
399 tip to the appearance of full suberization and a value of *k* beyond. Our simulations indicate that this
400 more realistic *k* representation does not impact the main conclusions on axial conductance (see
401 below) drawn from HydroRoot running with uniform *k* values.

402 **Assessing axial conductance**

403 Most often, axial conductance is roughly evaluated using the Hagen-Poiseuille law and there are only
404 a few instances where the axial conductance of roots was experimentally determined (Bramley et al.,
405 2009; Frensch and Steudle, 1989; Meunier et al., 2018). The overall literature data indicate that the
406 axial conductance can show a steep increase, from the root tip along the root axis, and most
407 importantly varies between plant species, by up to 5 orders of magnitude (Meunier et al., 2018).

408 Here, we investigated the importance of axial conductance in the context of highly branched
409 root systems. One first challenge was to develop a method for measuring *K* profiles throughout such
410 complex root systems, where axial flow measurements in individual thin root axes are not feasible.
411 However, microscopic observations suggested that *K* profile may be similar between root orders. This
412 allowed us to reduce the problem to only one *K* profile. The cut-and-flow approach provided an
413 efficient method, where the impact of multiple sections in roots of different orders was analyzed
414 through a complex parameter optimization. We note that, because of its design, the cut-and-flow
415 approach preferentially captures the features of axial transport and not radial transport. This is due
416 to the fact that the progressive increase in sap flow observed upon successive cuts, which result in a
417 progressive decrease in root surface, essentially reflects xylem vessel opening and suppression of
418 resistance of corresponding root tips.

419 Surprisingly, the experimentally determined *K* profile indicated values that were up to 10
420 times lower than concomitant estimates using anatomical measurements together with Hagen-
421 Poiseuille law. (Frensch and Steudle, 1989) and (Sanderson et al., 1988) also found that the measured
422 values were 2-5 times lower than the calculated ones, in maize and barley (*Hordeum vulgare*) roots,
423 respectively. Thus, it is likely that Hagen-Poiseuille estimates of single vessel conductance overlook
424 the resistance due to connections between finite vessel elements, to possible vascular constrictions
425 at the sites of root ramifications, or xylem surface properties (Sanderson et al., 1988; Shane et al.,
426 2000). As elegantly modelled by (Bouda et al., 2019), the failure of Hagen-Poiseuille estimates may
427 also be due to the functioning of xylem as a network integrating resistive connections between
428 functional vessels of distinct sizes.

429 Here, we further explored the importance of root axial conductance in a set of RSAs that
430 were built, by extension, on well-defined parameters captured in real plants. Our analyses which
431 extend the theoretical study of (Bouda et al., 2018), show that highly branched root systems can
432 show pronounced axial limitation for water transport. Firstly, J_V(P) showed a typical saturation in long
433 root systems (with primary root length > 14 cm)(Figure 5B) which somewhat reflects the plateau
434 shown by *K* along root length (Figures 2C). Increased root branching, while increasing the root
435 surface to the same extent as root length, may not necessarily reveal an axial limitation in the first
436 place (Figure 5C). However, spatially defined sensitivity analysis showed that hydraulic limitation due

437 to xylem transport can occur along the whole root axis (Figure 6D). This may typically happen at the
438 base of highly branched RSAs which convey converging flows from multiple root axes. Thus, although
439 root tips truly represent particular sites for hydraulic limitation, our analyses show that the hydraulic
440 load is somewhat spread over the whole root architecture. In other terms, the large metaxylem
441 vessels present at root bases are not as oversized as initially claimed (Steudle and Peterson, 1998). A
442 trade-off likely occurs on this trait as big vessels typically increase vulnerability of vascular tissues to
443 cavitation (Tyree et al., 1994).

444 The conceptualization of water transport through sequential radial and axial water transport
445 has somewhat led to independent estimates and functional analyses of the two processes. This
446 approach may be misleading as this and a previous study show that water transport is actually co-
447 limited by radial and axial conductances (Figure 6A) (Zarebanadkouki et al., 2016). As a consequence,
448 experimental determination of either one of these components strongly depends on the accuracy by
449 which the other component is evaluated or truly measured. In physiological terms, our work
450 indicates that real root systems can act on multiple cues to alter their water capacity. Interestingly,
451 conductivity of the radial pathway can be adjusted over short or medium term through aquaporin
452 regulation or root suberization whereas changes in RSA or vascular structures occur during much
453 longer (days) adaptive responses of the root. Yet, these distinct traits have surely to be coordinately
454 regulated, to ensure that root hydraulic architecture properly matches the plant's environmental
455 conditions and developmental stages. ABA was recently shown to play such a coordinating role under
456 water stress (Rosales et al., 2019).

457 **Deciphering complex root phenotypes**

458 Another major focus of our work was to work out the organizing principles of fully grown Arabidopsis
459 root systems and dissect their branching properties. First, we showed that steady-state lateral root
460 formation on a parent axis occurs over time and space in pretty well determined patterns that can be
461 characterized using two constant parameters, nude tip length and average internode length. Yet, the
462 growth and arrest of lateral roots appeared as a highly stochastic process. Overall, this process was
463 encapsulated in specific length laws thereby defining a complex pattern comprising several orders of
464 lateral roots. In addition, our data set allowed to generate a set of virtual RSAs that covers real RSAs
465 of distinct Arabidopsis genotypes. Conversely, it was critical for us to develop tools that would allow
466 identifying the branching profiles of specific genotypes. Here, we show that intercept number
467 profiles allow such kind of rapid and discriminative overview of RSA organization.

468 Earlier work has shown that defect in ESKIMO1 function results in xylem collapse. This
469 phenotype was tentatively associated with a reduced Lp_r (Lefebvre et al., 2011). Since then, ESKIMO1
470 was shown to function as a xylan-specific *O*-acetyl transferase during secondary cell wall synthesis

471 (Grantham et al., 2017; Yuan et al., 2013). Due to pleiotropic effects of cell wall alteration, *esk1*
472 mutants also show enhanced ABA accumulation (Lefebvre et al., 2011) and constitutive defense
473 responses (Escudero et al., 2017), which could both interfere with tissue hydraulics. Here, we chose
474 *esk1* genotypes as typically complex cases and used our full set of hydraulic and architectural
475 phenotyping and modelling approaches to revisit their root water uptake properties. In agreement
476 with early anatomical work on xylem defects in this genotype, our study provides a quantitative
477 estimate of reduction in axial conductance. Our analysis also pointed to a probable decrease in radial
478 conductance (Figure 7D) and profound changes in root architecture (Figures 7A and B). Thus, the
479 reduced water uptake capacity of *esk1* results from more complex root alterations than initially
480 thought. This example emphasizes the power of model-assisted hydraulic phenotyping which will
481 prove extremely valuable in support of quantitative genetic analyses of root hydraulics (Shahzad et
482 al., 2016; Tang et al., 2018). Along these lines, the MECHA model was recently used to infer distinct
483 radial hydraulic profiles present in maize roots, either wild-type or with deregulated Plasma
484 membrane Intrinsic Protein 2;5 (PIP;2;5) (Ding et al., 2020).
485
486 In conclusion, we have developed a model-assisted pipeline for accurate dissection of root hydraulic
487 architectures in complex, highly branched root systems. While much emphasis has been put so far on
488 aquaporin-mediated control of radial transport, our approach points to the complementary
489 importance of axial hydraulic conductance. Drawbacks in inferring this conductance from anatomical
490 measurements and the common idea that it is only limiting in root tips have led to underestimating
491 its importance. As a consequence, RSA is most often analyzed as the root foraging capacity for water
492 whereas it can be associated with true hydraulic limitations. More generally, we have developed
493 here a toolbox that can be used for dissecting the multiple root alterations that may interfere with
494 root uptake capacity, in different genotypes (this work) and, by extension, in various environmental
495 conditions. In particular, our study brings key tools to investigate, in Arabidopsis and possibly other
496 species, the impact on root hydraulic architecture of environmental factors (e.g. drought) or
497 hormones (e.g. ABA) acting on xylem differentiation (Ramachandran et al., 2020).
498

499 **Materials and methods**

500 **Plant culture**

501 Arabidopsis (*Arabidopsis thaliana*) seeds were surface sterilized (7min incubation in 86% (v/v)
502 ethanol and 0.03% (v/v) chlorine followed by 4 washes with 70% (v/v) ethanol) and germinated onto
503 a half-strength Murashige and Skoog medium with 0.9% (w/v)agar in square petri plates. Plates were
504 incubated in a growth chamber with 70% humidity, 16h light, 21°C for germination, and kept vertical
505 for 10 days. Seedlings were then transferred to a hydroponic culture medium (1.25 mM KNO_3, 0.75
506 mM $MgSO_4$, 1.5 mM, $Ca(NO_3)_2$, 0.5 mM KH_2PO_4, 50 µM FeEDTA, 50 µM H_3BO_3, 12 µM $MnSO_4$, 0.70
507 µM $CuSO_4$, 1 µM $ZnSO_4$, 0.24 µM MoO_4Na_2, and 100 µM Na_2SiO_3) for 9-10 additional days in the same
508 growth chamber. Columbia (Col-0) (N70000), *eskimo1-1* (Xin and Browse, 1998) and *eskimo1-5*
509 (SALK_089531)(Bouchabke-Coussa et al., 2008) plants were used in this study.

510 **Digitalizing of root architectures**

511 Excised root systems were spread out in a Petri dish containing a thin film of water, and gently
512 brushed prior to being digitized at 600-900ppi with a desktop scanner. Images were analyzed with
513 ImageJ software. For a given axis, internodes and lateral roots were traced back with straight or
514 segmented lines, which were then saved in the ROI manager. This procedure was applied for the
515 primary root as well as each lateral root carrying lateral roots, which resulted in a table containing
516 the internodes and lateral roots length for each branched root.

517 **Hagen-Poiseuille law estimate of axial conductance**

518 The axial conductance along a root axis was estimated from direct observations of xylem vessels,
519 using the Hagen-Poiseuille law applied to elliptic conduits. Root segments from the primary root, and
520 first and second order lateral roots were sampled every 2 cm, embedded in 7% (w/v) low-melting
521 agarose and sliced with a vibratome. Slices were imaged under an optical microscope and xylem
522 vessel dimensions were measured (Supplemental Figure 1A). Since vessel sections were not always
523 circular but possibly oblong, vessel conductance (in $m^4.s^{-1}.MPa^{-1}$) was computed according to the
524 general formula for elliptic conduit conductance (Lewis and Boose, 1995):

$$K = \frac{(\pi \times a^3 \times b^3)}{64 \times \eta \times (a^2 + b^2)}$$

525 where a and b are long and short axis diameters (m), respectively, and η is the viscosity of water
526 (1.10^{-3} Pa.s at 20°C). In all cases, a was less than two times b.

527 **Root water transport measurements**

528 Root water transport was measured on de-topped plants with a set of pressure chambers, as in
529 (Javot et al., 2003). The hypocotyl of an excised root system was inserted into an adapter and sealed
530 within the pressure chamber lid seal with silicone (Coltene Whaledent, France). The root was then
531 placed into the pressure chamber in a container filled with filtered (20 µm) hydroponic solution. The
532 adapter was connected to a flowmeter (Bronkhorst, France) in order to record the flow of sap from
533 the hypocotyl. After a first pressurization of 10min at 0.35 MPa, three successive flow measurements
534 were taken at 0.32, 0.16 and 0.24 MPa. A linear fit of the flow-to-pressure relationship (with $0.92 < r^2$
535 < 0.99) was used to deduce the sap flow at 0.3 MPa [Jv(0.3 MPa)].

536 **Modeling principles**

537 The HydroRoot model was developed in a Python programming language, as a component of the
538 OpenAlea platform (Pradal et al., 2008; Pradal et al., 2015). HydroRoot uses a Multiscale Tree Graph
539 (MTG) (Godin and Caraglio, 1998) to represent root hydraulic architecture, which consists of the
540 topology of a root system (branching positions, root lengths, root radii, etc.) and its hydraulic
541 structure (local radial and axial conductivities). The RSML format (Lobet et al., 2015) is used to import
542 and export the data to/from the HydroRoot model. The model is open source and available through
543 its public repository (https://github.com/openalea/hydroroot).

544 The hydraulic aspects of HydroRoot consisted in two main components: the radial water flow
545 between the bathing solution and the xylem vessels and the axial transport through the xylem
546 vessels. Following Doussan and colleagues (Doussan et al., 1998a; Doussan et al., 1998b), the root
547 was discretized as a network of elementary segments consisting of a microcircuit containing both
548 radial (k_i) and axial (K_i) hydraulic conductances (Figure 1C). The local radial flux was written as
549 $j_i = k_i(\psi_{e_i} - \psi_i)S_i$ and the local axial flow as $J_i = K_i\ (\psi_{out} - \psi_i)/L_i$, S_i and L_i being the surface
550 area and the length of the elementary segments, respectively. By analogy with Ohm's law, both
551 $1/(k_iS_i)$ and L_i/K_i may be modeled as electric resistances, and the hydraulic architecture may be
552 assimilated to an electrical network (Doussan et al., 1998a; Prusinkiewicz et al., 2007). According to
553 the boundary conditions (uniform pressure around the root and atmospheric pressure at its base),
554 we are able to calculate the equivalent resistance of the network and then calculate the outflow rate.
555 In brief, let us consider an elementary segment *i*, with $R_i = L_i/K_i$ and $r_i = 1/(k_iS_i)$ as axial and
556 radial resistances, respectively. Its equivalent resistance R_{eq_i} is calculated as follows, assuming that
557 the apical equivalent resistance $R_{eq_{i-1}}$ is known:

$$\frac{1}{R_{eq_i}} = \frac{1}{R_{eq_{i-1}} + r_i} + \frac{1}{R_i}$$

558 By implementing this equation, step by step from the tips, and by considering a branched root as a
559 parallel network, we end up with an equivalent resistance for the whole network, and as a
560 consequence, an equivalent hydraulic conductance K_{eq} (Albasha et al., 2019; Prusinkiewicz et al.,
561 2007). The basal outgoing flux (J_v) is then calculated according to:

$$J_{\mathrm{v}} = K_{eq}(\psi_e - \psi_{base})$$

562

563 **Cut-and-flow experiments**

564 An entire root system was excised and inserted into a pressure chamber, and water transport was
565 measured as explained above, to check for the linearity of the flow-to-pressure relationship, but with
566 a 10 µm filtered solution. If correct, the pressure was set to 0.3 MPa and the sap flow was recorded.
567 After 3-5 min, the pressure was released and the root system was taken out of the pressure chamber
568 and laid onto a 12x12cm Petri dish filled with filtered hydroponic solution. All roots were stretched
569 and aligned thereby allowing all longest root tip segments to be sectioned with a fresh razor blade, at
570 1-3cm from the tip of the longest root. The remaining root system was put back in the pressure
571 chamber at 0.3 MPa and flow measurement resumed for another 3-5 min. These steps
572 (Supplemental Figure 2) were repeated 3 to 8 times with the remaining tip segments of the root
573 system being cut each time according to the same principle. Sap flow measured at 0.3 MPa for each
574 cut step was then averaged, and plotted against the cut position on the primary root (See Figure 2B
575 as an example).

576 At each step, the released root segments and the remaining basal part of the root were
577 digitized and processed to reconstruct the initial architecture of the measured root (Supplemental
578 Figure 2). For each cut, roots segments were sorted in decreasing order of their total length (segment
579 length plus the sum of its lateral root length, if any) and positioned accordingly on the primary root.
580 Due to its diameter, the primary root was easily identified and could be attributed correctly for each
581 cut. This allowed us to determine the position of each cut along the primary axis, and therefore
582 reconstruct the whole RSA.

583 The final step of the whole procedure consisted in adjusting radial (*k*) and axial (*K*) conductances, to
584 fit the sap flow measured after each cut. As mentioned above, *K* varies along each root axis with the
585 distance to the tip. Here, *K* was represented as a linear piecewise function of nine points for an axis
586 length up to 19.75 cm which corresponds to the longest root among those analyzed for anatomical
587 data (Figure 2C). *K* was therefore represented by up to nine parameters. The radial conductivity *k*,
588 which is set uniform in our model, represented an additional parameter. Consequently, up to ten
589 parameters had to be adjusted from a data set of four to nine measurements. The system being
590 underdetermined, we constrained the first derivative of *K* between two consecutive points to a

minimum of -3.10^{-11} m^2.s^{-1}.MPa^{-1}. This negative value represents the minimum observed on the lowess smoothing (Figure 2C). The fit was then performed by minimizing the sum of square of the residuals. The averaged radial conductivity from ten Col-0 plants (Table 1), k_{ini}, and the nine axial conductance data points from the lowess fit (Figure 2C), K_{ini}, were set as initial parameters. The most effective procedure was obtained following these steps:

- k_1 and K_1 were first estimated by adjusting two multiplying factors, *ax* and *ar*, with lower bounds of 10^{-20}, such that $k_1 = ar \times k_{\mathrm{ini}}$ and $K_1 = ax \times K_{\mathrm{ini}}$;
- keeping k_1, the axial conductance points were then adjusted (with the constraint above and with a non-negative lower bound) from K_1, leading to K_2;
- keeping K_2, the radial conductivity was then adjusted from k_1 without bounds neither constraint, leading to k_2;
- the *k* and *K* adjustment loop (steps 2 and 3) was repeated until the variation in radial conductivity falls below 10^{-10} m.s^{-1}.MPa^{-1}.

We used the function optimize.minimize of the SciPy Python library to perform these minimizations. The minimizations 1 and 2 were done with the default solver according to bounds and constraints whereas the minimization of the radial conductivity (step 3) was done with the "Nelder-Mead" solver. The robustness of the fitting procedure was eventually tested by starting from different initial parameters (Supplemental Figure 3).

Statistical Analysis

All data sets were obtained in at least four independent biological repeats (plant cultures) with the indicated total number of plants. Pairwise comparisons of model parameters were performed using a Student *t* test ($P < 0.05$).

Accession Numbers

Accession number of *ESK1* is At3g55990.

Supplemental Data

Supplemental Figure S1. Parametrization of root axial conductance using Hagen-Poiseuille law.

Supplemental Figure S2. Experimental details on the cut-and-flow procedure.

Supplemental Figure S3. Robustness of axial conductance curve estimation procedure.

Supplemental Figure S4. Influence of a two-step radial conductivity profile on simulated root water uptake.

624 **Supplemental Figure S5.** Relationship between cumulated number of intercepts and integrative
625 properties of RSA.
626 **Supplemental Figure S6.** Dual dependency of J_v(P) on radial (*k*) and axial conductance (*K*).
627 **Supplemental Figure S7.** Effects of varying axial conductance profiles (*ax*) on local axial flow (*J*).
628 **Supplemental Figure S8.** Sensitivity analysis of J_v(0.3MPa) to RSA parameters in two distinct hydraulic
629 settings.
630 **Supplemental Table S1.** Parameters of HydroRoot model.
631
632

Funding

This work was supported in part by the Agence Nationale de la Recherche (ANR-11-BSV6-018) and the European Research Council (ERC) under the European Union's Horizon 2020 research and innovation programme (Grant Agreement ERC-2017-ADG-788553).

Table

Table 1: Measured architectural parameters and calculated elementary hydraulic radial conductance (*k*) of individual root systems. Water flow was measured using the pressure chamber technique in excised root systems from the indicated individual plants (2 biological replicates). RSAs were then exhaustively analyzed. The table summarizes integrated parameters from these measurements and the *k* values calculated using HydroRoot to match the measured water flows. The axial conductance was calibrated according to Hagen-Poiseuille law, and the same lowess fit profile, as shown in supplemental Figure 1, was used for all RSAs.

Plant number	Total length (m)	Surface area (10^{-4} m²)	Calculated *k* (10^{-8} m s^{-1} MPa^{-1})
#1	1.63	4.63	3.39
#2	1.88	5.18	7.08
#3	1.60	4.48	8.70
#4	0.71	2.20	5.59
#5	1.88	5.10	13.12
#6	1.12	3.36	8.30
#7	2.13	6.03	19.22
#8	2.11	6.05	22.13
#9	0.76	2.49	12.76
#10	0.78	2.59	4.03

Figure legends.

Figure 1. Modelling water transport in real RSAs.

(**A**) Representative RSA of a 21-day-old Arabidopsis plant grown in hydroponics. The excised root system was spread out in a petri dish and scanned. For clarity, the primary root, the first order and second order lateral roots are shown in blue, green and red, respectively. Scale bar: 10mm (**B**) Bi-dimensional representation of the same digitized RSA. Note that the emergence angle of root segments is arbitrarily set. Same color conventions as in A. Scale bar: 10mm (**C**) Schematic representation of an elementary root segment of rank *i* consisting of a derivative microcircuit containing both radial (k_i) and axial (K_i) hydraulic conductances. Each segment is connected with the root bathing solution (exterior, at Ψ_e water potential) and basal and apical neighboring segments (at Ψ_i and Ψ_{i+1} water potentials, respectively, except for the last segments). Combination of k_i and Ψ_e-Ψ_i, or K_i and Ψ_i–Ψ_{i+1} yield segment water uptake (j_i) and overall flow through the segment (J_i), respectively. (**D**) Elementary root segments are inserted into a dynamical Multiscale Tree Graph (MTG) builder of RSA to yield the HydroRoot model. The inset shows the specific case of a root ramification.

Figure 2. Determination of axial and radial conductances using cut-and-flow experiments.

(**A**) Kinetic measurement of pressure-induced sap flow (J_v) during a representative cut-and-flow experiment. J_v (black trace) was measured at constant pressure (magenta trace; P= 0.3 MPa). The intermittent drops in pressure (P) correspond to the maneuvers for opening the chamber and partial ablation of the root system. (**B**) Corresponding plot of J_v as a function of the root length that was cut from the primary root tip. (**C**) Profile of axial conductance (*K*) along the root axis as determined after parameter adjustment in cut-and-flow experiments. Data from 10 individual Col-0 plants, each being identified by a specific color. The figure shows (in magenta) the median *K* curve (solid line) and the 95% confidence interval (dashed lines). For reference, the lowess *K* profile and corresponding 95% confidence interval, as determined using Hagen-Poiseuille law (See Supplemental Figure 1b), are drawn in grey solid and dotted lines, respectively. (**D**) Mean values of radial conductance (k ± SE, n =10) as determined by model inversion, using Hagen-Poiseuille law or cut-and-flow experiments for evaluation of *K*. The two values are statistically different (Student *t* test; $P<0.01$).

Figure 3. Organizing principles of Col-0 RSA.

(**A**) Profile of lateral formation along the parental root axis. The dots show the cumulated number of lateral roots formed at the indicated distance from the root tip, in individual primary (black) and first order lateral (grey) roots. (**B**) Length of lateral root as a function of distance to tip of parental root.

We observed that the absolute lengths of first order lateral roots (*i.e.* carried by the primary root) were very similar between plants of a same age, despite the variations in length shown by the primary root. Thus, plotting lateral root length as a function of the relative distance to the tip of the bearing axis provides a comprehensive description of lateral root length repartition. This representation was conserved in second order lateral roots, whose length was referred to the longest first order lateral. (A) and (B) show cumulated data from 13 individual primary roots (black) and 9 first order lateral roots (grey). (**C**) Representative examples of simulated RSAs in (from left to right) the 25 percentile, median, and 75 percentile of total root length. Same color code for the primary root, the first order and second order lateral roots as in Figure 1.

Figure 4. Intercept number profiles in real and simulated RSAs.

(**A**) Total number of intercepted roots at the indicated distance from the root base. Continuous lines correspond to experimental measurements of two real RSAs entirely digitized while dashed lines correspond to discrete measurements of two other real RSAs. The grey area delineates the whole set of intercept number curves derived from 9520 simulated RSAs. Data are presented in a limited range of distances from tip (10-80 mm), to match the discrete experimental measurements. (**B**) Profiles of first and second order intercepted lateral roots. Data from a RSA digitized from a real plant showing that the total intercept number curve (orange, continuous) can be decomposed into three curves representing the primary root (blue, dashed), and the first (green, dashed, one dot) and second (magenta, dashed two dots) order lateral roots. (**C**) Relationship between total root length in 10 individual real plants (pink squares) and their close simulated RSAs (grey circles), screened by an absolute normalized difference in the intercepts at 10, 20, 30, 45, 60 and 80mm from the tip. See example in Supplemental Figure 3B.

Figure 5. Sensitivity analysis of pressure-induced sap flow to RSA parameters.

(**A**) Root surface-to-flow relationship. The figure shows pressure-induced flow simulations (J_V(0.3MPa)) for 9520 RSAs harboring three distinct hydraulic configurations derived from cut-and-flow experiments (i) low (blue): minimal experimental *k* (9.86 10^{-8} m.s^{-1}.MPa^{-1}) and all values of median *K* profile reduced two-fold (*ax*=0.5) (ii) intermediate (brown), mean *k* value (32.76 10^{-8} m.s^{-1}.MPa^{-1}) and median *K* profile (iii) high (green): maximal experimental *k* (71.43 10^{-8} m.s^{-1}.MPa^{-1}) and all values of median *K* profile enhanced two-fold (*ax*=2). J_V(0.3MPa) and root surface measured in 20 real RSAs (Table 1, Figure 2D) are shown as black dots. (**B**) Primary root length-to-flow relationship in 9520 simulated RSAs harboring a mean *k* value (32.76 10^{-8} m.s^{-1}.MPa^{-1}) and median *K* profile. The median response curve is shown as a solid orange line. (**C**) Dependency of J_V(0.3MPa) on average

internode length. Same procedures and conventions as in (B). (**D**) Relationship between nude tip length and J_V(0.3MPa). Same procedures and conventions as in (B).

Figure 6. Sensitivity analysis of pressure-induced sap flow to hydraulic parameters.

(**A**) Dual dependency of J_v(0.3MPa) on radial (*k*) and axial conductance (*K*). The latter is expressed as a multiplying factor (*ax*) applied to the median *K* profile. The figure shows J_V(0.3MPa) variations in a representative RSA. (**B**) Dependency of J_v(0.3MPa) on *k* in a set of 9520 RSAs, with fixed *K* (*ax*=1). The median response curve is shown as a solid orange line. (**C**) Dependency of J_v(0.3MPa) on axial conductance (*ax*) in a same set of 9520 RSAs, with fixed *k* (32.76 10^{-8} $m.s^{-1}.MPa^{-1}$). (**D**) Effects of varying axial conductance profiles (*ax*) on primary root axial flow (*J*) at the indicated distance from root tip. The figure shows simulations for the same RSA as in A (solid lines) or an unbranched (cylindric) root (dotted lines). Orange: *ax*=0.95; light blue: *ax*= 0.75; green: *ax*=0.5; magenta: *ax*= 0.25; blue: *ax*=0.05. All flow values are normalized with respect to the local flow observed in the same root and same position at *ax*=1. (**E**) Heat map representation of local radial flows for three levels of axial conductance (*ax*).

Figure 7. Root architecture and hydraulic phenotyping of *esk1* mutants.

(**A**) Total number of intercepted roots at the indicated distance from root base in Col-0 (black, *n*= 6), *esk1.1* (green, *n*= 7) and *esk1.5* (blue, *n*= 7). The figure shows, for each genotype, the mean curve and the envelope delineated by the 95% confidence interval for the number of intercepts at every mm. (**B**) Representative RSAs of Col-0, *esk1.1* and *esk1.5* plants. The primary root, the first order and second order lateral roots are shown in blue, green and red, respectively. (**C**) Profile of axial conductance (*K*) along the root axis as determined from cut-and-flow experiments in *esk1.1* (green, *n*= 5) and *esk1.5* (blue, *n*= 7). The figure shows, for each genotype, measurements on individual plants and the corresponding median curve. The median curve of Col-0 (grey) is redrawn from Figure 2C. (**D**) Corresponding radial conductivity values (*k* ± SE) (Col-0: *n* = 10; *esk1-1* : *n*= 5; *esk1.5* : *n* = 7).

References

Albasha, R., Fournier, C., Pradal, C., Chelle, M., Prieto, J.A., Louarn, G., Simonneau, T., and Lebon, E. (2019). HydroShoot: a functional-structural plant model for simulating hydraulic structure, gas and energy exchange dynamics of complex plant canopies under water deficit—application to grapevine (*Vitis vinifera*). in silico Plants *1*, diz007.

Barrowclough, D.E., Peterson, C.A., and Steudle, E. (2000). Radial hydraulic conductivity along developing onion roots. J Exp Bot *51*, 547-557.

Bouchabke-Coussa, O., Quashie, M.L., Seoane-Redondo, J., Fortabat, M.N., Gery, C., Yu, A., Linderme, D., Trouverie, J., Granier, F., Téoulé, E.*, et al.* (2008). ESKIMO1 is a key gene involved in water economy as well as cold acclimation and salt tolerance. BMC Plant Biol *8*, 125.

Bouda, M., Brodersen, C., and Saiers, J. (2018). Whole root system water conductance responds to both axial and radial traits and network topology over natural range of trait variation. J Theor Biol *456*, 49-61.

Bouda, M., Windt, C.W., McElrone, A.J., and Brodersen, C.R. (2019). In vivo pressure gradient heterogeneity increases flow contribution of small diameter vessels in grapevine. Nat Commun *10*, 5645.

Boursiac, Y., Boudet, J., Postaire, O., Luu, D.T., Tournaire-Roux, C., and Maurel, C. (2008). Stimulus-induced downregulation of root water transport involves reactive oxygen species-activated cell signalling and plasma membrane intrinsic protein internalization. Plant J *56*, 207-218.

Boursiac, Y., Chen, S., Luu, D.-T., Sorieul, M., van den Dries, N., and Maurel, C. (2005). Early effects of salinity on water transport in *Arabidopsis* roots. Molecular and cellular features of aquaporin expression. Plant Physiol *139*, 790-805.

Bramley, H., Turner, N.C., Turner, D.W., and Tyerman, S.D. (2009). Roles of morphology, anatomy, and aquaporins in determining contrasting hydraulic behavior of roots. Plant Physiol *150*, 348-364.

Calvo-Polanco, M., Ribeyre, Z., Dauzat, M., Reyt, G., Hidalgo-Shrestha, C., Diehl, P., Frenger, M., Simonneau, T., Muller, B., Salt, D.E.*, et al.* (2021). Physiological roles of Casparian strips and suberin in the transport of water and solutes. New Phytol *232*, 2295-2307.

Campilho, A., Nieminen, K., and Ragni, L. (2020). The development of the periderm: the final frontier between a plant and its environment. Curr Opin Plant Biol *53*, 10-14.

Couvreur, V., Faget, M., Lobet, G., Javaux, M., Chaumont, F., and Draye, X. (2018). Going with the flow: multiscale insights into the composite nature of water transport in roots. Plant Physiol *178*, 1689-1703.

Danjon, F., and Reubens, B. (2008). Assessing and analyzing 3D architecture of woody root systems, a review of methods and applications in tree and soil stability, resource acquisition and allocation. Plant Soil *303*, 1–34.

Di Pietro, M., Vialaret, J., Li, G., Hem, S., Rossignol, M., Maurel, C., and Santoni, V. (2013). Coordinated post-translational responses of aquaporins to abiotic and nutritional stimuli in *Arabidopsis* roots. Mol Cell Proteomics *12*, 3886-3897.

Ding, L., Milhiet, T., Couvreur, V., Nelissen, H., Meziane, A., Parent, B., Aesaert, S., Van Lijsebettens, M., Inze, D., Tardieu, F.*, et al.* (2020). Modification of the expression of the aquaporin *Zm*PIP2;5 affects water relations and plant growth. Plant Physiol *182*, 2154-2165.

Doblas, V.G., Geldner, N., and Barberon, M. (2017). The endodermis, a tightly controlled barrier for nutrients. Curr Opin Plant Biol *39*, 136-143.

Doussan, C., Pages, L., and Vercambre, G. (1998a). Modelling of the hydraulic architecture of root systems: an integrated approach to water absorption - Model description. Ann Bot *81*, 213-223.

Doussan, C., Pierret, A., Garrigues, E., and Pages, L. (2006). Water uptake by plant roots: II – Modelling of water transfer in the soil root-system with explicit account of flow within the root system – Comparison with experiments. Plant Soil *283*, 99-117.

Doussan, C., Vercambre, G., and Pages, L. (1998b). Modelling of the hydraulic architecture of root systems: an integrated approach to water absorption - Distribution of axial and radial conductances in maize. Ann Bot *81*, 225-232.

Draye, X., Kim, Y., Lobet, G., and Javaux, M. (2010). Model-assisted integration of physiological and environmental constraints affecting the dynamic and spatial patterns of root water uptake from soils. J Exp Bot *8*, 2145-2155.

Escudero, V., Jorda, L., Sopena-Torres, S., Melida, H., Miedes, E., Munoz-Barrios, A., Swami, S., Alexander, D., McKee, L.S., Sanchez-Vallet, A.*, et al.* (2017). Alteration of cell wall xylan acetylation triggers defense responses that counterbalance the immune deficiencies of plants impaired in the beta-subunit of the heterotrimeric G-protein. Plant J *92*, 386-399.

Foster, K.J., and Miklavcic, S.J. (2016). Modeling root zone effects on preferred pathways for the passive transport of ions and water in plant roots. Front Plant Sci *7*, 914.

Frensch, J., Hsiao, T.C., and Steudle, E. (1996). Water and solute transport along developing maize roots. Planta *198*, 348-355.

Frensch, J., and Steudle, E. (1989). Axial and radial hydraulic resistance to roots of maize (*Zea mays* L.). Plant Physiol *91*, 719-726.

Gambetta, G.A., Fei, J., Rost, T.L., Knipfer, T., Matthews, M.A., Shackel, K.A., Walker, M.A., and McElrone, A.J. (2013). Water uptake along the length of grapevine fine roots: developmental anatomy, tissue-specific aquaporin expression, and pathways of water transport. Plant Physiol *163*, 1254-1265.

Godin, C., and Caraglio, Y. (1998). A multiscale model of plant topological structures. J Theor Biol *191*, 1-46.

Godin, C., Costes, E., and Sinoquet, H. (1999). A method for describing plant architecture which integrates topology and geometry. Ann Bot *84*, 343–357.

Grantham, N.J., Wurman-Rodrich, J., Terrett, O.M., Lyczakowski, J.J., Stott, K., Iuga, D., Simmons, T.J., Durand-Tardif, M., Brown, S.P., Dupree, R.*, et al.* (2017). An even pattern of xylan substitution is critical for interaction with cellulose in plant cell walls. Nat Plants *3*, 859-865.

Heymans, A., Couvreur, V., and Lobet, G. (2021). Combining cross-section images and modeling tools to create high-resolution root system hydraulic atlases in Zea mays. Plant Direct *5*, e334.

Hosy, E., Vavasseur, A., Mouline, K., Dreyer, I., Gaymard, F., Poree, F., Boucherez, J., Lebaudy, A., Bouchez, D., Very, A.A.*, et al.* (2003). The Arabidopsis outward K+ channel GORK is involved in regulation of stomatal movements and plant transpiration. Proc Natl Acad Sci USA *100*, 5549-5554.

Javaux, M., Couvreur, V., Vanderborght, J., and Vereecken, H. (2013). Root water uptake: from three-dimensional biophysical processes to macroscopic modeling approaches. Vadose Zone J *12*.

Javot, H., Lauvergeat, V., Santoni, V., Martin-Laurent, F., Guclu, J., Vinh, J., Heyes, J., Franck, K.I., Schäffner, A.R., Bouchez, D.*, et al.* (2003). Role of a single aquaporin isoform in root water uptake. Plant Cell *15*, 509-522.

Jones, H., Leigh, R.A., Jones, R.G.W., and Tomos, A.D. (1988). The integration of whole-root and cellular hydraulic conductivities in cereal roots. Planta *174*, 1-7.

Klein, S.P., Schneider, H.M., Perkins, A.C., Brown, K.M., and Lynch, J.P. (2020). Multiple integrated root phenotypes are associated with improved drought tolerance. Plant Physiol *183*, 1011-1025.

Knipfer, T., and Fricke, W. (2011). Water uptake by seminal and adventitious roots in relation to whole-plant water flow in barley (*Hordeum vulgare* L.). J Exp Bot *62*, 717-733.

Lee, S.H., Chung, G.C., Jang, J.Y., Ahn, S.J., and Zwiazek, J.J. (2012). Overexpression of PIP2;5 aquaporin alleviates effects of low root temperature on cell hydraulic conductivity and growth in *Arabidopsis*. Plant Physiol *159*, 479-488.

Lefebvre, V., Fortabat, M.-N., Ducamp, A., North, H.M., Maia-Grondard, A., Trouverie, J., Boursiac, Y., Mouille, G., and Durand-Tardif, M. (2011). ESKIMO1 disruption in *Arabidopsis* alters vascular tissue and impairs water transport. PLoS One *6*, e16645.

Lewis, A.M., and Boose, E.R. (1995). Estimating volume flow rates through xylem conduits. Am J Bot *82*, 1112-1116.

Lobet, G., Pound, M.P., Diener, J., Pradal, C., Draye, X., Godin, C., Javaux, M., Leitner, D., Meunier, F., Nacry, P.*, et al.* (2015). Root system markup language: toward a unified root architecture description language. Plant Physiol *167*, 617-627.

Lucas, M., Guedon, Y., Jay-Allemand, C., Godin, C., and Laplaze, L. (2008). An auxin transport-based model of root branching in Arabidopsis thaliana. PLoS One *3*, e3673.

Lynch, J.P. (2013). Steep, cheap and deep: an ideotype to optimize water and N acquisition by maize root systems. Ann Bot *112*, 347-357.

Macho-Rivero, M.A., Camacho-Cristobal, J.J., Herrera-Rodriguez, M.B., Muller, M., Munne-Bosch, S., and Gonzalez-Fontes, A. (2017). Abscisic acid and transpiration rate are involved in the response to boron toxicity in Arabidopsis plants. Physiol Plant *160*, 21-32.

Maurel, C., and Nacry, P. (2020). Root architecture and hydraulics converge for acclimation to changing water availability. Nat Plants *6*, 744-749.

Meunier, F., Couvreur, V., Draye, X., Vanderborght, J., and Javaux, M. (2017a). Towards quantitative root hydraulic phenotyping: novel mathematical functions to calculate plant-scale hydraulic parameters from root system functional and structural traits. J Math Biol *75*, 1133-1170.

Meunier, F., Couvreur, V., Draye, X., Zarebanadkouki, M., Vanderborght, J., and Javaux, M. (2017b). Water movement through plant roots - exact solutions of the water flow equation in roots with linear or exponential piecewise hydraulic properties. Hydrol Earth Syst Sc *21*, 6519-6540.

Meunier, F., Draye, X., Vanderborght, J., Javaux, M., and Couvreur, V. (2017c). A hybrid analytical-numerical method for solving water flow equations in root hydraulic architectures. Appl Math Model *52*, 648-663.

Meunier, F., Zarebanadkouki, M., Ahmed, M.A., Carminati, A., Couvreur, V., and Javaux, M. (2018). Hydraulic conductivity of soil-grown lupine and maize unbranched roots and maize root-shoot junctions. J Plant Physiol *227*, 31-44.

Pascut, F.C., Couvreur, V., Dietrich, D., Leftley, N., Reyt, G., Boursiac, Y., Calvo-Polanco, M., Casimiro, I., Maurel, C., Salt, D.E.*, et al.* (2021). Non-invasive hydrodynamic imaging in plant roots at cellular resolution. Nat Commun *12*, 4682.

Postaire, O., Tournaire-Roux, C., Grondin, A., Boursiac, Y., Morillon, R., Schäffner, T., and Maurel, C. (2010). A PIP1 aquaporin contributes to hydrostatic pressure-induced water transport in both the root and rosette of Arabidopsis. Plant Physiol *152*, 1418-1430.

Pradal, C., Dufour-Kowalski, S., Boudon, F., Fournier, C., and Godin, C. (2008). OpenAlea: a visual programming and component-based software platform for plant modelling. Function Plant Biol *35*, 751-760.

Pradal, C., Fournier, C., Valduriez, P., and Cohen-Boulakia, S. (2015). OpenAlea: scientific workflows combining data analysis and simulation. Paper presented at: International Conference on Scientific and Statistical Database Management (San Diego).

Prusinkiewicz, P., Allen, M., Escobar-Gutierrez, A., and DeJong, T.M. (2007). Numerical methods for transport-resistance sink-source allocation models. Frontis *22*, 123-137.

Ramachandran, P., Augstein, F., Nguyen, V., and Carlsbecker, A. (2020). Coping with water limitation: hormones that modify plant root xylem development. Front Plant Sci *11*, 570.

Ranathunge, K., and Schreiber, L. (2011). Water and solute permeabilities of *Arabidopsis* roots in relation to the amount and composition of aliphatic suberin. J Exp Bot *62*, 1961-1974.

Rosales, M.A., Maurel, C., and Nacry, P. (2019). Abscisic acid coordinates dose-dependent developmental and hydraulic responses of roots to water deficit. Plant Physiol *180*, 2198-2211.

Sanderson, J., Whitbread, F.C., and Clarkson, D.T. (1988). Persistent Xylem Cross-Walls Reduce the Axial Hydraulic Conductivity in the Apical 20 Cm of Barley Seminal Root Axes - Implications for the Driving Force for Water-Movement. Plant Cell and Environment *11*, 247-256.

Shahzad, Z., Canut, M., Tournaire-Roux, C., Martinière, A., Boursiac, Y., Loudet, O., and Maurel, C. (2016). A potassium-dependent oxygen sensing pathway regulates plant root hydraulics. Cell *167*, 87-98.

Shane, M.W., McCully, M.E., and Canny, M.J. (2000). Architecture of branch-root junctions in maize: Structure of the connecting xylem and the porosity of pit membranes. Ann Bot *85*, 613-624.

Steudle, E. (2001). The Cohesion-Tension mechanism and the acquisition of water by plant roots. Annu Rev Plant Physiol Plant Mol Biol *52*, 847-875.

Steudle, E., and Jeschke, W.D. (1983). Water transport in barley roots - Measurements of root pressure and hydraulic conductivity of roots in parallel with turgor and hydraulic conductivity of root cells Planta *158*, 237-248.

Steudle, E., and Peterson, C.A. (1998). How does water get through roots? J Exp Bot *49*, 775-788.

Sutka, M., Li, G., Boudet, J., Boursiac, Y., Doumas, P., and Maurel, C. (2011). Natural variation of root hydraulics in *Arabidopsis* grown in normal and salt stress conditions. Plant Physiol *155*, 1264-1276.

Tang, N., Shahzad, Z., Lonjon, F., Loudet, O., Vailleau, F., and Maurel, C. (2018). Natural variation at *XND1* impacts root hydraulics and trade-off for stress responses in Arabidopsis. Nat Commun *9*, 3884.

Tixier, A., Cochard, H., Badel, E., Dusotoit-Coucaud, A., Jansen, S., and Herbette, S. (2013). *Arabidopsis thaliana* as a model species for xylem hydraulics: does size matter? J Exp Bot *64*, 2295-2305.

Tournaire-Roux, C., Sutka, M., Javot, H., Gout, E., Gerbeau, P., Luu, D.T., Bligny, R., and Maurel, C. (2003). Cytosolic pH regulates root water transport during anoxic stress through gating of aquaporins. Nature *425*, 393-397.

Tyree, M.T., Davis, S.D., and Cochard, C. (1994). Biophysical perspectives of xylem evolution: is there a tradeoff of hydraulic efficiency for vulnerability to dysfunction? IAWA J *15*, 335-360.

Xin, Z., and Browse, J. (1998). *Eskimo1* mutants of Arabidopsis are constitutively freezing-tolerant. Proc Natl Acad Sci U S A *95*, 7799-7804.

Yang, Z., Sinclair, T.R., Zhu, M., Messina, C.D., Cooper, M., and Hammer, G.L. (2012). Temperature effect on transpiration response of maize plants to vapour pressure deficit. Env Exp Bot *78*, 157–162.

Yuan, Y., Teng, Q., Zhong, R., and Ye, Z.H. (2013). The Arabidopsis DUF231 domain-containing protein ESK1 mediates 2-O- and 3-O-acetylation of xylosyl residues in xylan. Plant Cell Physiol *54*, 1186-1199.

Zarebanadkouki, M., Kroener, E., Kaestner, A., and Carminati, A. (2014). Visualization of root water uptake: quantification of deuterated water transport in roots using neutron radiography and numerical modeling. Plant Physiol *166*, 487-499.

Zarebanadkouki, M., Meunier, F., Couvreur, V., Cesar, J., Javaux, M., and Carminati, A. (2016). Estimation of the hydraulic conductivities of lupine roots by inverse modelling of high-resolution measurements of root water uptake. Ann Bot *118*, 853-864.

Zwieniecki, M.A., Thompson, M.V., and Holbrook, N.M. (2003). Understanding the hydraulics of porous pipes: Tradeoffs between water uptake and root length utilization. J Plant Growth Regul *21*, 315-323.

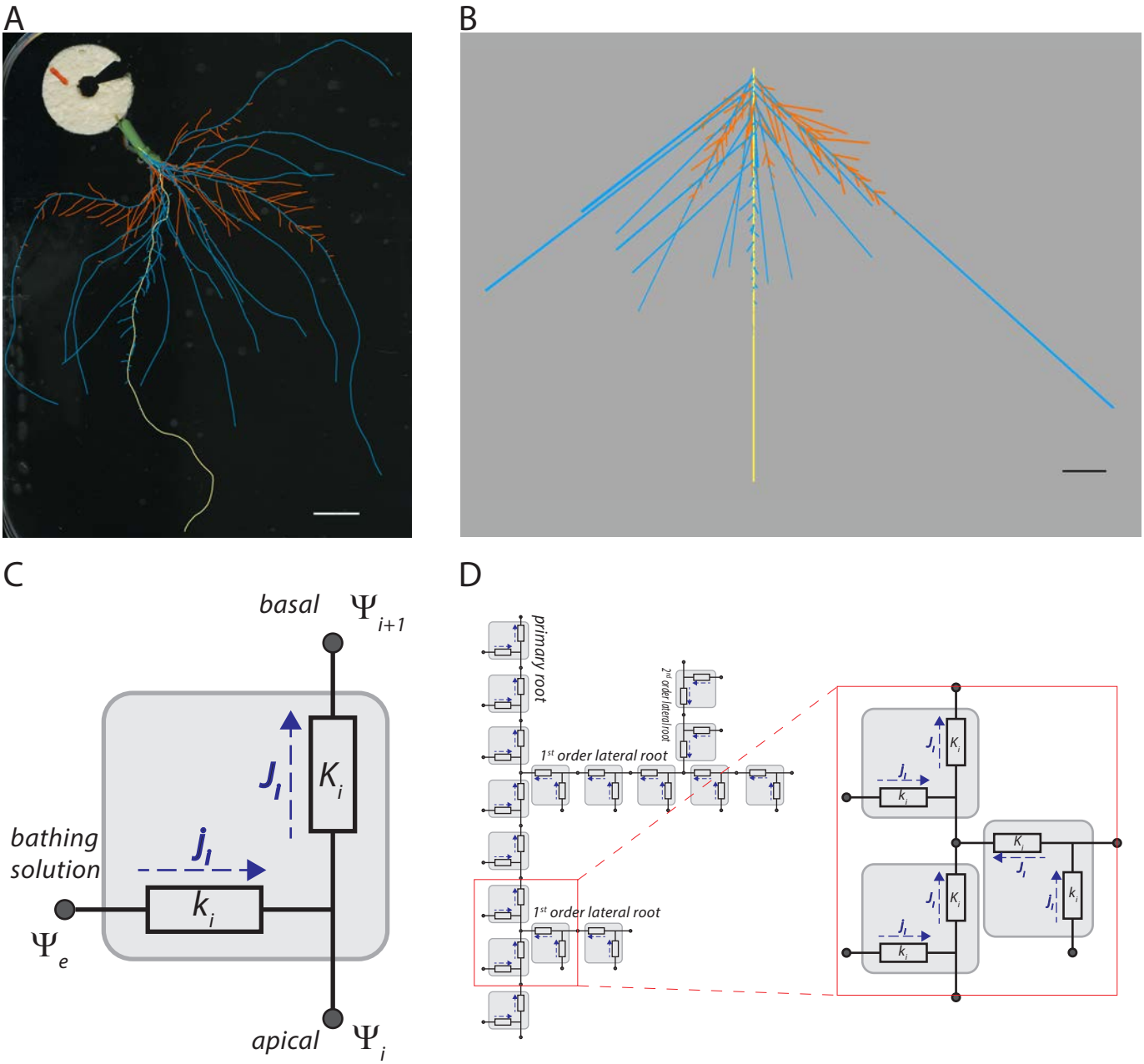

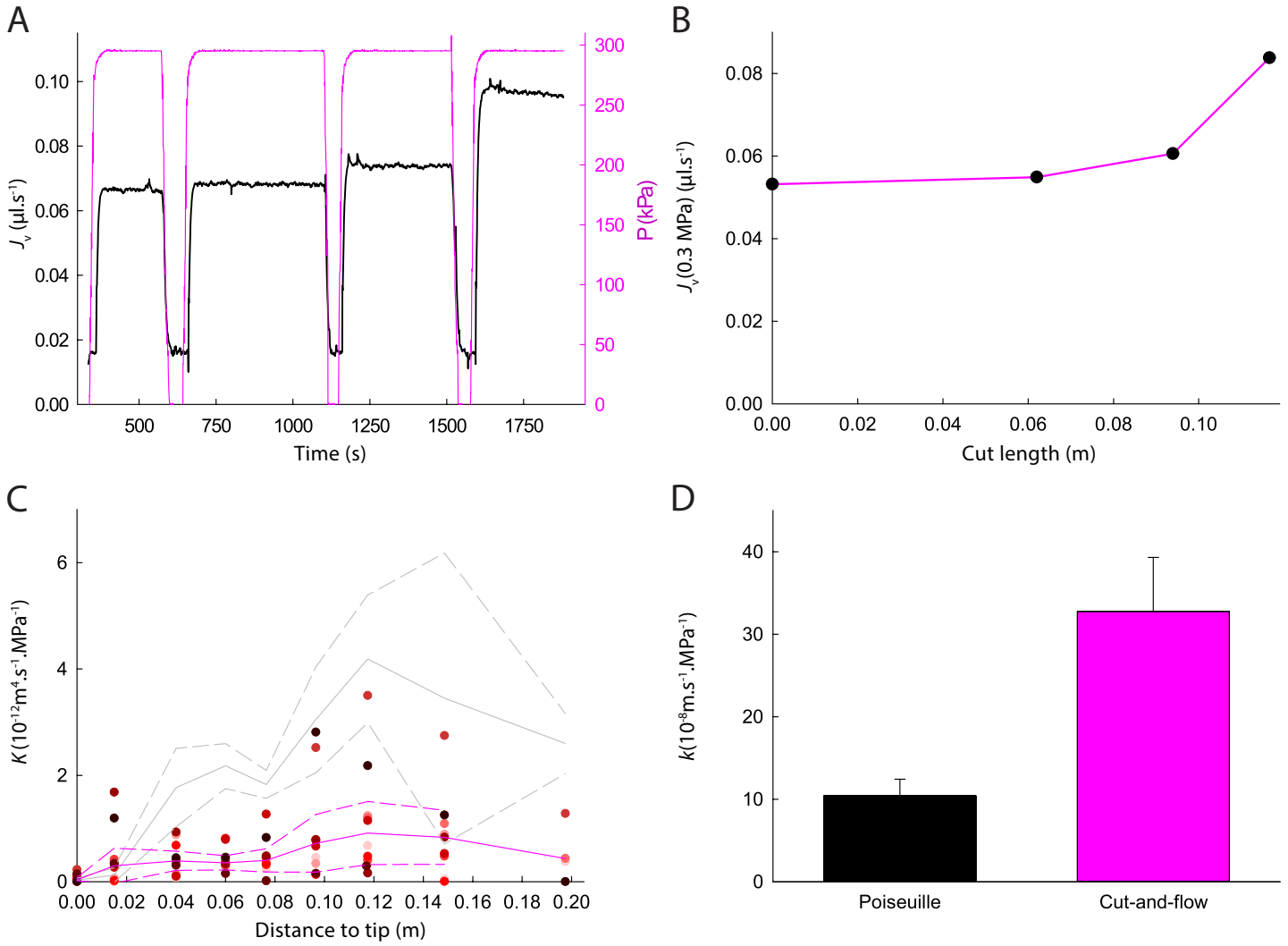

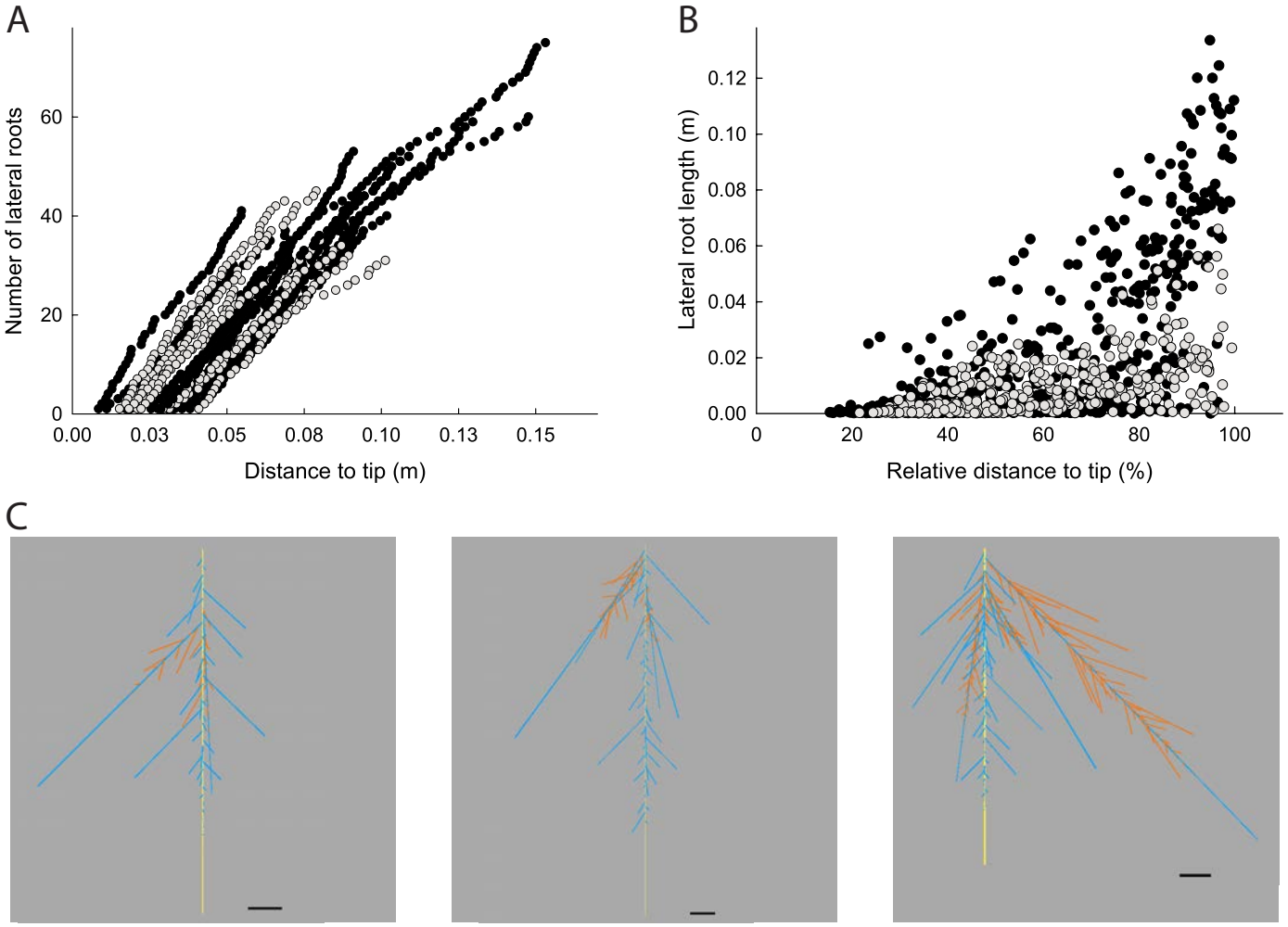

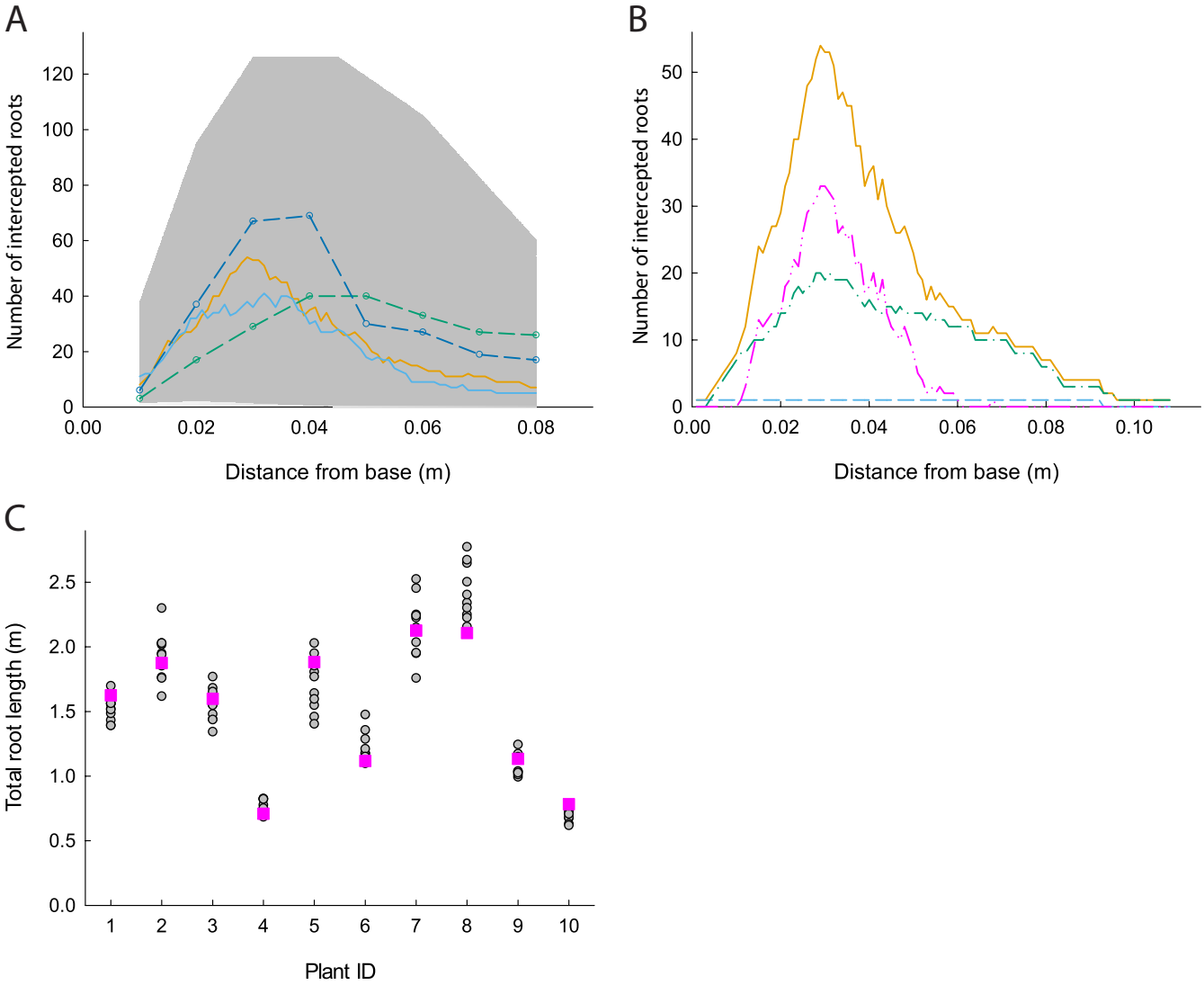

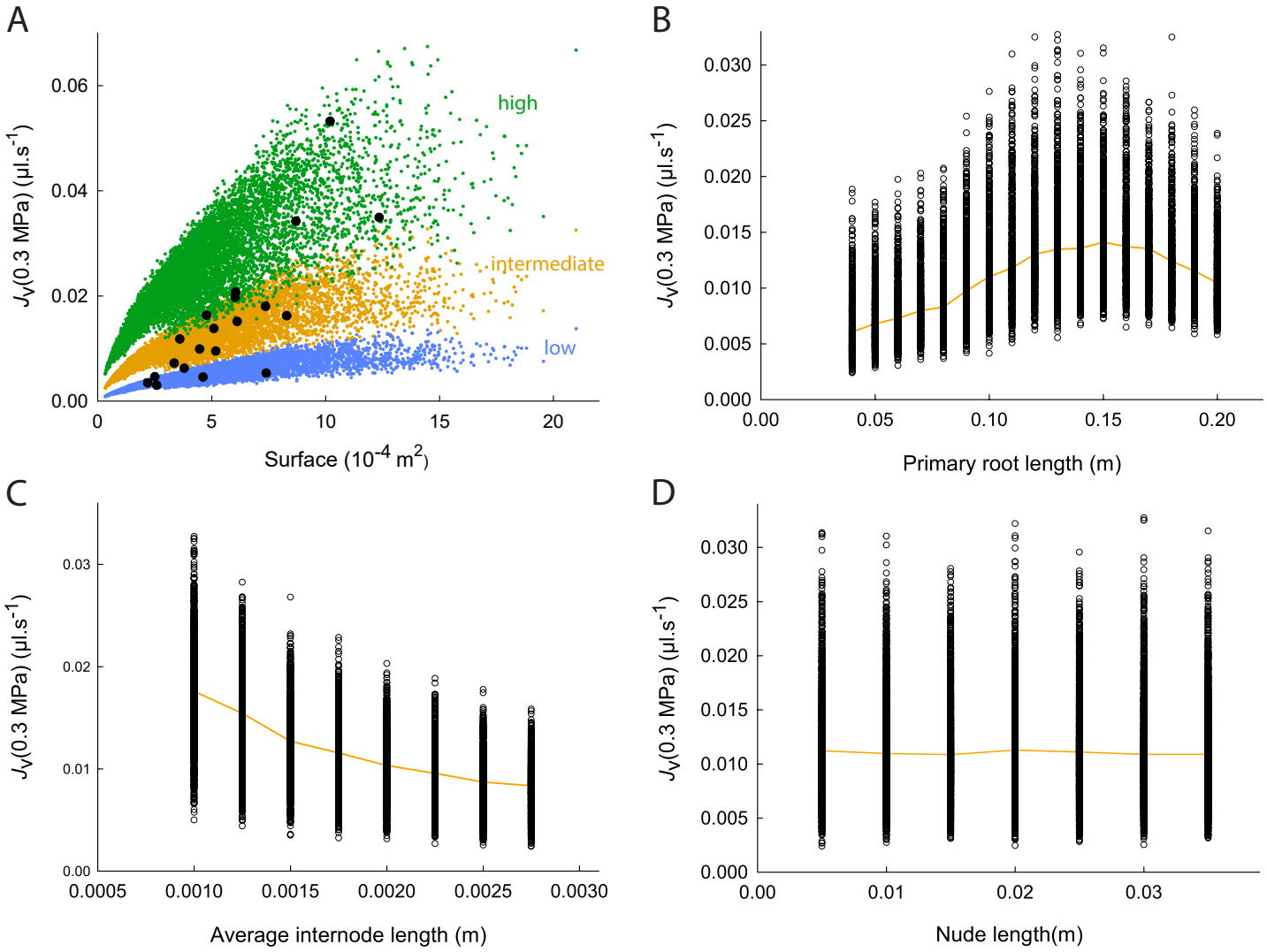

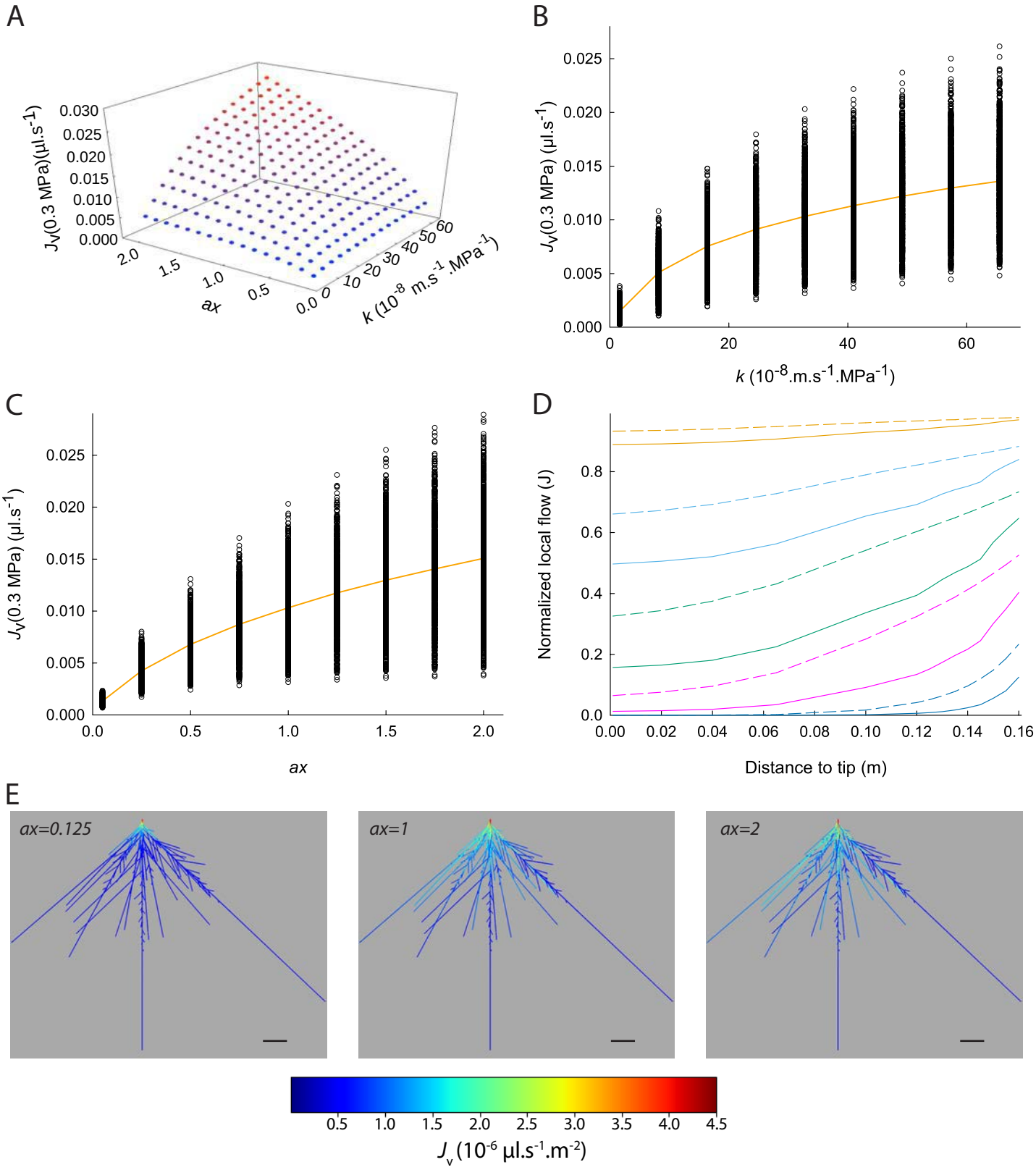

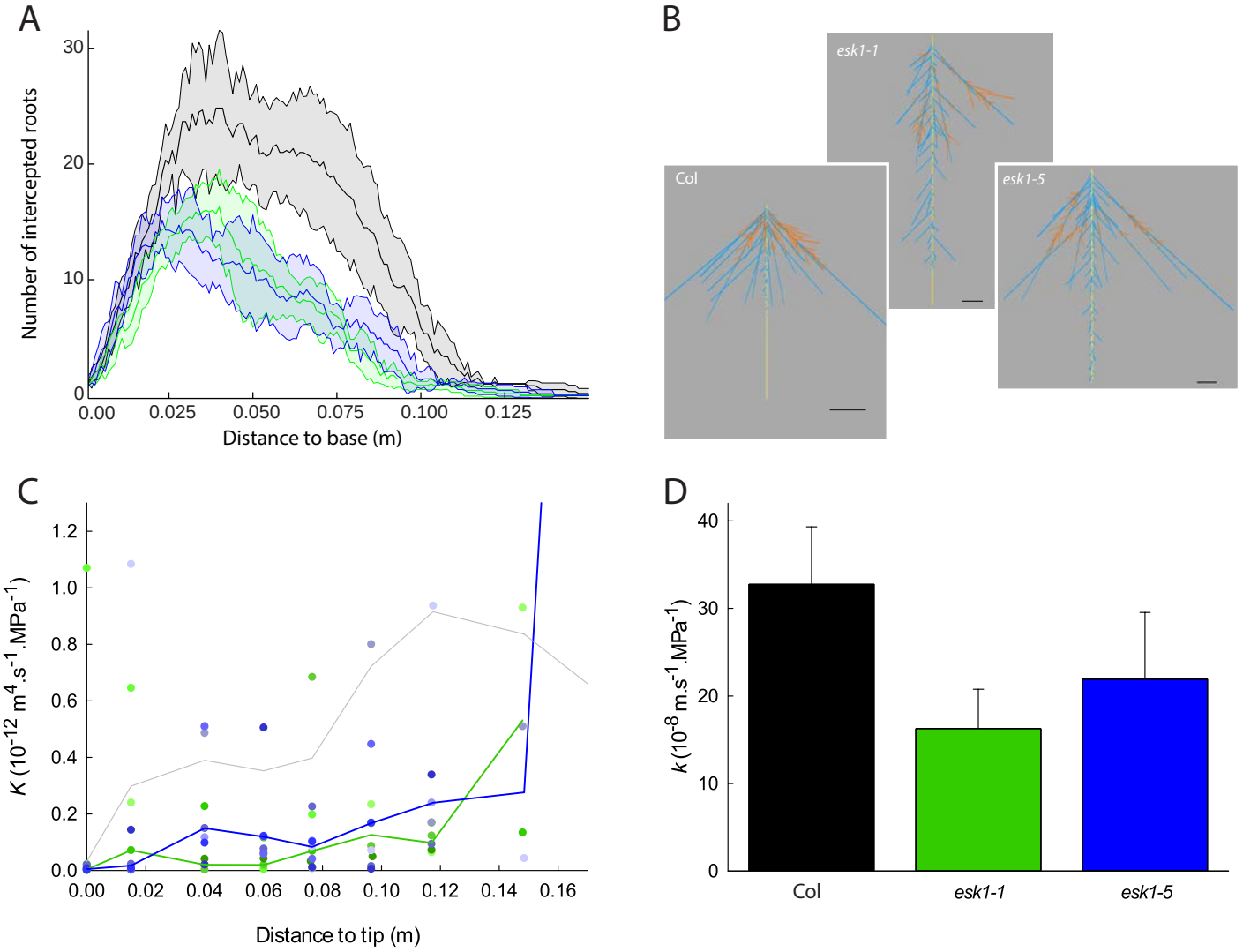

Parsed Citations

Albasha, R., Fournier, C., Pradal, C., Chelle, M., Prieto, J.A., Louarn, G., Simonneau, T., and Lebon, E. (2019). HydroShoot: a functional-structural plant model for simulating hydraulic structure, gas and energy exchange dynamics of complex plant canopies under water deficit-application to grapevine (Vitis vinifera). in silico Plants 1, diz007.
Google Scholar: Author Only Title Only Author and Title

Barrowclough, D.E., Peterson, C.A., and Steudle, E. (2000). Radial hydraulic conductivity along developing onion roots. J Exp Bot 51, 547-557.
Google Scholar: Author Only Title Only Author and Title

Bouchabke-Coussa, O., Quashie, M.L., Seoane-Redondo, J., Fortabat, M.N., Gery, C., Yu, A., Linderme, D., Trouverie, J., Granier, F., Téoulé, E., et al. (2008). ESKIMO1 is a key gene involved in water economy as well as cold acclimation and salt tolerance. BMC Plant Biol 8, 125.
Google Scholar: Author Only Title Only Author and Title

Bouda, M., Brodersen, C., and Saiers, J. (2018). Whole root system water conductance responds to both axial and radial traits and network topology over natural range of trait variation. J Theor Biol 456, 49-61.
Google Scholar: Author Only Title Only Author and Title

Bouda, M., Windt, C.W., McElrone, A.J., and Brodersen, C.R. (2019). In vivo pressure gradient heterogeneity increases flow contribution of small diameter vessels in grapevine. Nat Commun 10, 5645.
Google Scholar: Author Only Title Only Author and Title

Boursiac, Y., Boudet, J., Postaire, O., Luu, D.T., Tournaire-Roux, C., and Maurel, C. (2008). Stimulus-induced downregulation of root water transport involves reactive oxygen species-activated cell signalling and plasma membrane intrinsic protein internalization. Plant J 56, 207-218.
Google Scholar: Author Only Title Only Author and Title

Boursiac, Y., Chen, S., Luu, D.-T., Sorieul, M., van den Dries, N., and Maurel, C. (2005). Early effects of salinity on water transport in Arabidopsis roots. Molecular and cellular features of aquaporin expression. Plant Physiol 139, 790-805.
Google Scholar: Author Only Title Only Author and Title

Bramley, H., Turner, N.C., Turner, D.W., and Tyerman, S.D. (2009). Roles of morphology, anatomy, and aquaporins in determining contrasting hydraulic behavior of roots. Plant Physiol 150, 348-364.
Google Scholar: Author Only Title Only Author and Title

Calvo-Polanco, M., Ribeyre, Z., Dauzat, M., Reyt, G., Hidalgo-Shrestha, C., Diehl, P., Frenger, M., Simonneau, T., Muller, B., Salt, D.E., et al. (2021). Physiological roles of Casparian strips and suberin in the transport of water and solutes. New Phytol 232, 2295-2307.
Google Scholar: Author Only Title Only Author and Title

Campilho, A., Nieminen, K., and Ragni, L. (2020). The development of the periderm: the final frontier between a plant and its environment. Curr Opin Plant Biol 53, 10-14.
Google Scholar: Author Only Title Only Author and Title

Couvreur, V., Faget, M., Lobet, G., Javaux, M., Chaumont, F., and Draye, X. (2018). Going with the flow: multiscale insights into the composite nature of water transport in roots. Plant Physiol 178, 1689-1703.
Google Scholar: Author Only Title Only Author and Title

Danjon, F., and Reubens, B. (2008). Assessing and analyzing 3D architecture of woody root systems, a review of methods and applications in tree and soil stability, resource acquisition and allocation. Plant Soil 303, 1–34.
Google Scholar: Author Only Title Only Author and Title

Di Pietro, M., Vialaret, J., Li, G., Hem, S., Rossignol, M., Maurel, C., and Santoni, V. (2013). Coordinated post-translational responses of aquaporins to abiotic and nutritional stimuli in Arabidopsis roots. Mol Cell Proteomics 12, 3886-3897.
Google Scholar: Author Only Title Only Author and Title

Ding, L., Milhiet, T., Couvreur, V., Nelissen, H., Meziane, A., Parent, B., Aesaert, S., Van Lijsebettens, M., Inze, D., Tardieu, F., et al. (2020). Modification of the expression of the aquaporin ZmPIP2;5 affects water relations and plant growth. Plant Physiol 182, 2154-2165.
Google Scholar: Author Only Title Only Author and Title

Doblas, V.G., Geldner, N., and Barberon, M. (2017). The endodermis, a tightly controlled barrier for nutrients. Curr Opin Plant Biol 39, 136-143.
Google Scholar: Author Only Title Only Author and Title

Doussan, C., Pages, L., and Vercambre, G. (1998a). Modelling of the hydraulic architecture of root systems: an integrated approach to water absorption - Model description. Ann Bot 81, 213-223.
Google Scholar: Author Only Title Only Author and Title

Doussan, C., Pierret, A., Garrigues, E., and Pages, L. (2006). Water uptake by plant roots: II – Modelling of water transfer in the soil root-system with explicit account of flow within the root system – Comparison with experiments. Plant Soil 283, 99-117.
Google Scholar: Author Only Title Only Author and Title

Doussan, C., Vercambre, G., and Pages, L. (1998b). Modelling of the hydraulic architecture of root systems: an integrated approach to water absorption - Distribution of axial and radial conductances in maize. Ann Bot 81, 225-232.
Google Scholar: Author Only Title Only Author and Title

Draye, X., Kim, Y., Lobet, G., and Javaux, M. (2010). Model-assisted integration of physiological and environmental constraints affecting the dynamic and spatial patterns of root water uptake from soils. J Exp Bot 8, 2145-2155.
Google Scholar: Author Only Title Only Author and Title

Escudero, V., Jorda, L., Sopena-Torres, S., Melida, H., Miedes, E., Munoz-Barrios, A., Swami, S., Alexander, D., McKee, L.S., Sanchez-Vallet, A., et al. (2017). Alteration of cell wall xylan acetylation triggers defense responses that counterbalance the immune deficiencies of plants impaired in the beta-subunit of the heterotrimeric G-protein. Plant J 92, 386-399.
Google Scholar: Author Only Title Only Author and Title

Foster, K.J., and Miklavcic, S.J. (2016). Modeling root zone effects on preferred pathways for the passive transport of ions and water in plant roots. Front Plant Sci 7, 914.
Google Scholar: Author Only Title Only Author and Title

Frensch, J., Hsiao, T.C., and Steudle, E. (1996). Water and solute transport along developing maize roots. Planta 198, 348-355.
Google Scholar: Author Only Title Only Author and Title

Frensch, J., and Steudle, E. (1989). Axial and radial hydraulic resistance to roots of maize (Zea mays L.). Plant Physiol 91, 719-726.
Google Scholar: Author Only Title Only Author and Title

Gambetta, G.A., Fei, J., Rost, T.L., Knipfer, T., Matthews, M.A., Shackel, K.A., Walker, M.A., and McElrone, A.J. (2013). Water uptake along the length of grapevine fine roots: developmental anatomy, tissue-specific aquaporin expression, and pathways of water transport. Plant Physiol 163, 1254-1265.
Google Scholar: Author Only Title Only Author and Title

Godin, C., and Caraglio, Y. (1998). A multiscale model of plant topological structures. J Theor Biol 191, 1-46.
Google Scholar: Author Only Title Only Author and Title

Godin, C., Costes, E., and Sinoquet, H. (1999). A method for describing plant architecture which integrates topology and geometry. Ann Bot 84, 343–357.
Google Scholar: Author Only Title Only Author and Title

Grantham, N.J., Wurman-Rodrich, J., Terrett, O.M., Lyczakowski, J.J., Stott, K., Iuga, D., Simmons, T.J., Durand-Tardif, M., Brown, S.P., Dupree, R., et al. (2017). An even pattern of xylan substitution is critical for interaction with cellulose in plant cell walls. Nat Plants 3, 859-865.
Google Scholar: Author Only Title Only Author and Title

Heymans, A., Couvreur, V., and Lobet, G. (2021). Combining cross-section images and modeling tools to create high-resolution root system hydraulic atlases in Zea mays. Plant Direct 5, e334.
Google Scholar: Author Only Title Only Author and Title

Hosy, E., Vavasseur, A., Mouline, K., Dreyer, I., Gaymard, F., Poree, F., Boucherez, J., Lebaudy, A., Bouchez, D., Very, A.A., et al. (2003). The Arabidopsis outward K+ channel GORK is involved in regulation of stomatal movements and plant transpiration. Proc Natl Acad Sci USA 100, 5549-5554.
Google Scholar: Author Only Title Only Author and Title

Javaux, M., Couvreur, V., Vanderborght, J., and Vereecken, H. (2013). Root water uptake: from three-dimensional biophysical processes to macroscopic modeling approaches. Vadose Zone J 12.
Google Scholar: Author Only Title Only Author and Title

Javot, H., Lauvergeat, V., Santoni, V., Martin-Laurent, F., Guclu, J., Vinh, J., Heyes, J., Franck, K.I., Schäffner, A.R., Bouchez, D., et al. (2003). Role of a single aquaporin isoform in root water uptake. Plant Cell 15, 509-522.
Google Scholar: Author Only Title Only Author and Title

Jones, H., Leigh, R.A., Jones, R.G.W., and Tomos, A.D. (1988). The integration of whole-root and cellular hydraulic conductivities in cereal roots. Planta 174, 1-7.
Google Scholar: Author Only Title Only Author and Title

Klein, S.P., Schneider, H.M., Perkins, A.C., Brown, K.M., and Lynch, J.P. (2020). Multiple integrated root phenotypes are associated with improved drought tolerance. Plant Physiol 183, 1011-1025.
Google Scholar: Author Only Title Only Author and Title

Knipfer, T., and Fricke, W. (2011). Water uptake by seminal and adventitious roots in relation to whole-plant water flow in barley

(Hordeum vulgare L.). J Exp Bot 62, 717-733.
Google Scholar: Author Only Title Only Author and Title

Lee, S.H., Chung, G.C., Jang, J.Y., Ahn, S.J., and Zwiazek, J.J. (2012). Overexpression of PIP2;5 aquaporin alleviates effects of low root temperature on cell hydraulic conductivity and growth in Arabidopsis. Plant Physiol 159, 479-488.
Google Scholar: Author Only Title Only Author and Title

Lefebvre, V., Fortabat, M.-N., Ducamp, A., North, H.M., Maia-Grondard, A., Trouverie, J., Boursiac, Y., Mouille, G., and Durand-Tardif, M. (2011). ESKIMO1 disruption in Arabidopsis alters vascular tissue and impairs water transport. PLoS One 6, e16645.
Google Scholar: Author Only Title Only Author and Title

Lewis, A.M., and Boose, E.R. (1995). Estimating volume flow rates through xylem conduits. Am J Bot 82, 1112-1116.
Google Scholar: Author Only Title Only Author and Title

Lobet, G., Pound, M.P., Diener, J., Pradal, C., Draye, X., Godin, C., Javaux, M., Leitner, D., Meunier, F., Nacry, P., et al. (2015). Root system markup language: toward a unified root architecture description language. Plant Physiol 167, 617-627.
Google Scholar: Author Only Title Only Author and Title

Lucas, M., Guedon, Y., Jay-Allemand, C., Godin, C., and Laplaze, L. (2008). An auxin transport-based model of root branching in Arabidopsis thaliana. PLoS One 3, e3673.
Google Scholar: Author Only Title Only Author and Title

Lynch, J.P. (2013). Steep, cheap and deep: an ideotype to optimize water and N acquisition by maize root systems. Ann Bot 112, 347-357.
Google Scholar: Author Only Title Only Author and Title

Macho-Rivero, M.A., Camacho-Cristobal, J.J., Herrera-Rodriguez, M.B., Muller, M., Munne-Bosch, S., and Gonzalez-Fontes, A. (2017). Abscisic acid and transpiration rate are involved in the response to boron toxicity in Arabidopsis plants. Physiol Plant 160, 21-32.
Google Scholar: Author Only Title Only Author and Title

Maurel, C., and Nacry, P. (2020). Root architecture and hydraulics converge for acclimation to changing water availability. Nat Plants 6, 744-749.
Google Scholar: Author Only Title Only Author and Title

Meunier, F., Couvreur, V., Draye, X., Vanderborght, J., and Javaux, M. (2017a). Towards quantitative root hydraulic phenotyping: novel mathematical functions to calculate plant-scale hydraulic parameters from root system functional and structural traits. J Math Biol 75, 1133-1170.
Google Scholar: Author Only Title Only Author and Title

Meunier, F., Couvreur, V., Draye, X., Zarebanadkouki, M., Vanderborght, J., and Javaux, M. (2017b). Water movement through plant roots - exact solutions of the water flow equation in roots with linear or exponential piecewise hydraulic properties. Hydrol Earth Syst Sc 21, 6519-6540.
Google Scholar: Author Only Title Only Author and Title

Meunier, F., Draye, X., Vanderborght, J., Javaux, M., and Couvreur, V. (2017c). A hybrid analytical-numerical method for solving water flow equations in root hydraulic architectures. Appl Math Model 52, 648-663.
Google Scholar: Author Only Title Only Author and Title

Meunier, F., Zarebanadkouki, M., Ahmed, M.A., Carminati, A., Couvreur, V., and Javaux, M. (2018). Hydraulic conductivity of soil-grown lupine and maize unbranched roots and maize root-shoot junctions. J Plant Physiol 227, 31-44.
Google Scholar: Author Only Title Only Author and Title

Pascut, F.C., Couvreur, V., Dietrich, D., Leftley, N., Reyt, G., Boursiac, Y., Calvo-Polanco, M., Casimiro, I., Maurel, C., Salt, D.E., et al. (2021). Non-invasive hydrodynamic imaging in plant roots at cellular resolution. Nat Commun 12, 4682.
Google Scholar: Author Only Title Only Author and Title

Postaire, O., Tournaire-Roux, C., Grondin, A., Boursiac, Y., Morillon, R., Schäffner, T., and Maurel, C. (2010). A PIP1 aquaporin contributes to hydrostatic pressure-induced water transport in both the root and rosette of Arabidopsis. Plant Physiol 152, 1418-1430.
Google Scholar: Author Only Title Only Author and Title

Pradal, C., Dufour-Kowalski, S., Boudon, F., Fournier, C., and Godin, C. (2008). OpenAlea: a visual programming and component-based software platform for plant modelling. Function Plant Biol 35, 751-760.
Google Scholar: Author Only Title Only Author and Title

Pradal, C., Fournier, C., Valduriez, P., and Cohen-Boulakia, S. (2015). OpenAlea: scientific workflows combining data analysis and simulation. Paper presented at: International Conference on Scientific and Statistical Database Management (San Diego).
Google Scholar: Author Only Title Only Author and Title

Prusinkiewicz, P., Allen, M., Escobar-Gutierrez, A., and DeJong, T.M. (2007). Numerical methods for transport-resistance sink-source allocation models. Frontis 22, 123-137.
Google Scholar: Author Only Title Only Author and Title

Ramachandran, P., Augstein, F., Nguyen, V., and Carlsbecker, A. (2020). Coping with water limitation: hormones that modify plant root xylem development. Front Plant Sci 11, 570.
Google Scholar: Author Only Title Only Author and Title

Ranathunge, K., and Schreiber, L. (2011). Water and solute permeabilities of Arabidopsis roots in relation to the amount and composition of aliphatic suberin. J Exp Bot 62, 1961-1974.
Google Scholar: Author Only Title Only Author and Title

Rosales, M.A., Maurel, C., and Nacry, P. (2019). Abscisic acid coordinates dose-dependent developmental and hydraulic responses of roots to water deficit. Plant Physiol 180, 2198-2211.
Google Scholar: Author Only Title Only Author and Title

Sanderson, J., Whitbread, F.C., and Clarkson, D.T. (1988). Persistent Xylem Cross-Walls Reduce the Axial Hydraulic Conductivity in the Apical 20 Cm of Barley Seminal Root Axes - Implications for the Driving Force for Water-Movement. Plant Cell and Environment 11, 247-256.
Google Scholar: Author Only Title Only Author and Title

Shahzad, Z., Canut, M., Tournaire-Roux, C., Martinière, A., Boursiac, Y., Loudet, O., and Maurel, C. (2016). A potassium-dependent oxygen sensing pathway regulates plant root hydraulics. Cell 167, 87-98.
Google Scholar: Author Only Title Only Author and Title

Shane, M.W., McCully, M.E., and Canny, M.J. (2000). Architecture of branch-root junctions in maize: Structure of the connecting xylem and the porosity of pit membranes. Ann Bot 85, 613-624.
Google Scholar: Author Only Title Only Author and Title

Steudle, E. (2001). The Cohesion-Tension mechanism and the acquisition of water by plant roots. Annu Rev Plant Physiol Plant Mol Biol 52, 847-875.
Google Scholar: Author Only Title Only Author and Title

Steudle, E., and Jeschke, W.D. (1983). Water transport in barley roots - Measurements of root pressure and hydraulic conductivity of roots in parallel with turgor and hydraulic conductivity of root cells Planta 158, 237-248.
Google Scholar: Author Only Title Only Author and Title

Steudle, E., and Peterson, C.A. (1998). How does water get through roots? J Exp Bot 49, 775-788.
Google Scholar: Author Only Title Only Author and Title

Sutka, M., Li, G., Boudet, J., Boursiac, Y., Doumas, P., and Maurel, C. (2011). Natural variation of root hydraulics in Arabidopsis grown in normal and salt stress conditions. Plant Physiol 155, 1264-1276.
Google Scholar: Author Only Title Only Author and Title

Tang, N., Shahzad, Z., Lonjon, F., Loudet, O., Vailleau, F., and Maurel, C. (2018). Natural variation at XND1 impacts root hydraulics and trade-off for stress responses in Arabidopsis. Nat Commun 9, 3884.
Google Scholar: Author Only Title Only Author and Title

Tixier, A., Cochard, H., Badel, E., Dusotoit-Coucaud, A., Jansen, S., and Herbette, S. (2013). Arabidopsis thaliana as a model species for xylem hydraulics: does size matter? J Exp Bot 64, 2295-2305.
Google Scholar: Author Only Title Only Author and Title

Tournaire-Roux, C., Sutka, M., Javot, H., Gout, E., Gerbeau, P., Luu, D.T., Bligny, R., and Maurel, C. (2003). Cytosolic pH regulates root water transport during anoxic stress through gating of aquaporins. Nature 425, 393-397.
Google Scholar: Author Only Title Only Author and Title

Tyree, M.T., Davis, S.D., and Cochard, C. (1994). Biophysical perspectives of xylem evolution: is there a tradeoff of hydraulic efficiency for vulnerability to dysfunction? IAWA J 15, 335-360.
Google Scholar: Author Only Title Only Author and Title

Xin, Z., and Browse, J. (1998). Eskimo1 mutants of Arabidopsis are constitutively freezing-tolerant. Proc Natl Acad Sci U S A 95, 7799-7804.
Google Scholar: Author Only Title Only Author and Title

Yang, Z., Sinclair, T.R., Zhu, M., Messina, C.D., Cooper, M., and Hammer, G.L. (2012). Temperature effect on transpiration response of maize plants to vapour pressure deficit. Env Exp Bot 78, 157–162.
Google Scholar: Author Only Title Only Author and Title

Yuan, Y., Teng, Q., Zhong, R., and Ye, Z.H. (2013). The Arabidopsis DUF231 domain-containing protein ESK1 mediates 2-O- and 3-O-acetylation of xylosyl residues in xylan. Plant Cell Physiol 54, 1186-1199.

Google Scholar: Author Only Title Only Author and Title

Zarebanadkouki, M., Kroener, E., Kaestner, A., and Carminati, A. (2014). Visualization of root water uptake: quantification of deuterated water transport in roots using neutron radiography and numerical modeling. Plant Physiol 166, 487-499.
Google Scholar: Author Only Title Only Author and Title

Zarebanadkouki, M., Meunier, F., Couvreur, V., Cesar, J., Javaux, M., and Carminati, A. (2016). Estimation of the hydraulic conductivities of lupine roots by inverse modelling of high-resolution measurements of root water uptake. Ann Bot 118, 853-864.
Google Scholar: Author Only Title Only Author and Title

Zwieniecki, M.A., Thompson, M.V., and Holbrook, N.M. (2003). Understanding the hydraulics of porous pipes: Tradeoffs between water uptake and root length utilization. J Plant Growth Regul 21, 315-323.
Google Scholar: Author Only Title Only Author and Title